

Exploring the nature of the jetted hybrid AGNs: PKS 2004-447, 3C 286, and PKS 0440-00 through the SED modeling

J. Luna-Cervantes,^{1*} A. Tramacere,² E. Benítez^{1†}

¹Universidad Nacional Autónoma de México, Instituto de Astronomía, AP 70-264, CDMX 04510, Mexico

²Department of Astronomy, University of Geneva, Ch. d'Ecogia 16, 1290 Versoix, Switzerland

Accepted XXX. Received YYY; in original form ZZZ

ABSTRACT

In this work, we explore the connection of three jetted γ -loud AGNs classes: Compact Steep-Spectrum Sources (CSS), Narrow-Line Seyfert 1 (NLS1), and Flat-Spectrum Radio Quasars, through the modeling of the spectral energy distribution (SED). We selected two sources identified as CSS/NLS1 hybrids, PKS 2004-440 and 3C 286. Additionally, we included the source PKS 0440-00, initially classified as an FSRQ in the first *Fermi*-LAT catalog, but recently reclassified as an NLS1. We present the results of their broadband SED modeling using a one-zone leptonic synchrotron-self Compton (SSC)+ external Compton (EC) model. By exploring the parameter space and investigating the disk-jet connection in these sources, we analyze their classification in a model-dependent way. Our findings reveal that modeling PKS 2004-447 at relatively large angles, as expected for CSS, results in an SSC-dominated inverse Compton emission. In contrast, at low observing angles, the inverse Compton emission is dominated by external photon fields. Both scenarios result in a jet with a low radiative power. For 3C 286 we found that using a one-zone model limits the jet viewing angle to $\sim 7^\circ$, mainly due to its impact on the γ -ray emission. Our model results show a magnetically dominated jet, consistent with γ -CSS sources. Our results suggest that PKS 0440-00, can be classified as a powerful γ -NLS1, characterized by high accretion power and a jet dominated by bulk motion, similar to FSRQs.

Key words: galaxies: active – galaxies:nuclei – galaxies: jets – galaxies:individual: PKS 2004-447 – galaxies:individual: 3C 286 – galaxies:individual: PKS 0440-00

1 INTRODUCTION

The radio-loud Active Galactic Nuclei (AGNs), also known as jetted AGNs by Padovani (2017), are divided into different classes, including blazars and radio galaxies. The orientation of relativistic jets in these AGNs, relative to our line of sight, can lead to different observed characteristics (Antonucci 1993; Urry & Padovani 1995). For instance, their small viewing angles in blazars can result in extreme variability and high polarization emission. Conversely, in radio galaxies, the orientation enables the observation of extended radio lobes. Additional classes of jetted AGNs were also identified as gamma-ray sources by the Large Area Telescope (LAT) on board the *Fermi* Gamma-Ray Space Telescope, in particular, some Narrow-line Seyfert 1 (NLS1) galaxies (e.g., Abdo et al. 2009a) and Compact-steep Spectrum Sources (CSS) (Abdollahi et al. 2020).

The formation of jets in AGNs is thought to be connected to a spinning, accreting supermassive black hole (SMBH), and the accretion disk formed by the falling material towards it. (e.g., Zeldovich & Novikov 1971; Rees 1978; Blandford et al. 2019). The intense magnetic fields near the black hole event horizon play a crucial role in the acceleration and collimation of particles into these relativistic

jets (e.g., Blandford & Znajek 1977; Begelman et al. 1984; Sikora & Begelman 2013).

Blazars are jetted AGNs known for their extreme and often variable emission across the electromagnetic spectrum, from radio to gamma-rays, harboring powerful and highly beamed relativistic jets (e.g. Blandford & Rees 1978; Böttcher 2007). Their multiwavelength spectral energy distribution (SED) exhibits a characteristic double hump shape dominated by non-thermal emission processes originating from the relativistic jet. Based on the rest-frame equivalent width (EW) of their optical emission lines, blazars are commonly divided into Flat spectrum radio quasars (FSRQ) with $EW > 5 \text{ \AA}$ and the BL Lac objects ($EW < 5 \text{ \AA}$). FSRQs are characterized by strong broad emission lines and a photon-rich environment, with a strong and efficient accretion disk (Best & Heckman 2012), while BL Lac objects show weak or absent emission lines, low-density photon environment and a disk accreting inefficiently onto the central SMBH (Sbarato et al. 2012).

NLS1s are identified by their optical spectrum, which exhibits broad and narrow emission lines. The criteria commonly used to define NLS1s include showing narrow $H\beta$ emission lines with $FWHM(H\beta) < 2000 \text{ km s}^{-1}$, weak [OIII] emission lines (with $[OIII]/H\beta < 3$), and the presence of strong FeII multiplets (Os-terbrock & Pogge 1985; Goodrich 1989).

The SED of NLS1 galaxies often shows strong thermal emission from the accretion disk and non-thermal emission from the jet. Only

* E-mail: jluna@astro.unam.mx

† E-mail: erika@astro.unam.mx

7% of the NLS1 are radio-loud (Komossa 2018), and within them, only a small fraction has been detected in gamma-rays. This fraction of NLS1 shows steep photon indices and high variability in the X-ray band, which corroborates the relatively low-mass black holes (typically $M_{\text{BH}} \lesssim 10^8 M_{\odot}$, in comparison with blazars, where $M_{\text{BH}} \lesssim 10^8\text{--}10^{10} M_{\odot}$), accreting at high Eddington rates¹ (Komossa 2018). Some authors have proposed that jetted NLS1s are the young counterpart of FSRQs and that those with misaligned relativistic jets may eventually evolve to form the parent population of FSRQs (see e.g., Berton et al. 2016; Foschini et al. 2017; Berton et al. 2021).

About 70% of the NLS1 are compact radio-emitters with steep spectra, showing a connection with the Compact steep-spectrum sources (CSS) (Komossa 2018). The link between NLS1 and CSS has been suggested by many authors (e.g., Komossa et al. 2006; Gu et al. 2015; Berton et al. 2016). The CSS are compact radio sources with a steep high-frequency spectrum in radio ($\alpha \geq 0.5$, $F_{\nu} \propto \nu^{-\alpha}$) with a turnover below ~ 400 MHz, characterized to have fully developed radio lobes and small projected linear size (< 20 kpc) which is considered to be an indicator of young age (Fanti et al. 1995; O’Dea 1998; Murgia et al. 1999). Many CSS sources are embedded in a dense interstellar medium with their jets vigorously interacting with it (see e.g., O’Dea & Saikia 2021).

The existence of sources that share properties associated with two classes (i.e., hybrids, in this case, NLS1s with blazar-like SEDs or radio characteristics similar to CSS), indicates a potential evolutionary connection between these jetted AGN classes, that could be understood in terms of a unification scenario (Berton et al. 2021). The shared underlying physical processes offer a unique opportunity to explore the interplay between accretion disks, relativistic jets, and surrounding matter in AGNs.

In this work, we investigate the parameter space obtained through the SED modeling of three jetted AGNs gamma-ray emitters, using the JetSeT framework, fitting the SED from radio to γ -rays with a one-zone leptonic SSC+EC model. We examine different models to fit the SEDs of the chosen sources. This approach allows us to explore the nature of the sources by testing different orientations of the jet and diverse black hole masses to get the best fit of the SEDs of the chosen sources. We then discuss the implications of the derived jet and disk properties, intending to identify signatures that associate the sources with a specific jetted AGN class or confirm their hybrid behavior. The selected sources include two objects previously classified as hybrid sources CSS/NLS1: PKS 2004-447 and 3C 286. We examine their similarities and differences with the NLS1 and CSS classes, exploring their classification. Additionally, PKS 0440-00 is incorporated into our analysis as a potential hybrid between the NLS1 and FSRQ classes. We present the best model for this source and discuss the feasibility of classifying it as NLS1 or proposing it as an FSRQ/NLS1 hybrid.

The paper is organized as follows: in Section 2 we present the three selected sources. In Section 3, we describe the multiwavelength data employed to construct the SED for each source. In section 4 we describe the leptonic model used to fit the broadband SED. The main results are presented in Section 5. A detailed discussion of the nature of the three sources is given in Section 6, and we summarize our conclusions in Section 7. Throughout this paper we use a Hubble constant $H_0 = 67.8 \text{ km s}^{-1} \text{ Mpc}^{-1}$, $\Omega_m = 0.307$, and $\Omega_{\Lambda} = 0.692$ (Planck Collaboration et al. 2014).

2 THE SAMPLE

We have selected three γ -ray-emitting jetted AGNs, being classified either as Compact Steep Sources (CSS), Narrow Line Seyfert 1 (NLS1), or Flat Spectrum Radio Quasars (FSRQ). Two sources are already being classified as CSS/NLS1, i.e. hybrid sources, namely, PKS 2004-447 ($z = 0.24$) (Berton et al. 2021) and 3C 286 ($z = 0.849$) (Berton et al. 2017). The hybrid nature was established based on their radio properties similar to CSS and optical emission lines in agreement with the NLS1 class. The third source, PKS 0440-00 ($z = 0.844$), initially detected in the γ -rays by the *Fermi* satellite during its first year of operation, is known to be a bright FSRQ (Abdo et al. 2010). However, Foschini et al. (2021) have found NLS1 characteristics on this source, in particular the $\text{FWHM}(H\beta) = 1700 \text{ km s}^{-1}$, which associates PKS 0440-00 with the NLS1 class, according to the $\text{FWHM}(H\beta) < 2000 \text{ km s}^{-1}$ criterion.

3 MULTIWAVELENGTH DATA

For each of the sources, we built the average SED, covering the radio band up to γ -rays, using data collected from the ASI Science Data Center (ASDC) SED builder².

The data collected for PKS 2004-447 spans from August 2008 to May 2012, with γ -rays data from the *Fermi*-LAT Third Source Catalog (3FGL). Based on the *Fermi* light curve data³, the source did not exhibit significant activity during this period. The SED is representative of an average activity state. For 3C 286, we use simultaneous observations from the *Swift* UVOT and XRT, taken in August 2020, analyzed by Yao & Komossa (2021). The SED covers observations from radio to γ -rays between August 2008 and August 2021, including data from the Atacama Large Millimeter/submillimeter Array (ALMA) Calibrator Source Catalogue⁴. Despite the long time range, the source showed steady activity, particularly in γ -rays, with a variability index of 2.92, as reported in the fourth *Fermi* Large Area Telescope catalog (4FGL). For PKS 0440-00, the collected data spans from March 2007 to February 2010, using γ -rays data from the 2 Year *Fermi*-LAT Sources Catalog (2FGL). Even when the source had significant gamma-ray activity during the period covered by the SED, there were no critical flux changes according to the *Fermi* light curve. Moreover, we studied the average activity state of the source.

4 MODELING THE BROADBAND SED

We modeled the SED of the sources with a numerical one-zone leptonic model implemented in Jets SED modeler and fitting Tool (JetSeT) (Tramacere et al. 2009, 2011; Tramacere 2020). The model accounts for synchrotron radiation and inverse Compton (IC) scattering of both, synchrotron radiation (Synchrotron Self-Compton, SSC) and external photon fields (External Compton, EC), to fit the SED from radio to the γ -rays. The seed photons for the EC process are photons generated by the accretion disk surrounding the black hole (BH) and reflected towards the jet by the BLR and the dusty torus. The γ -ray emission from FSRQ, is well-fitted by EC processes (Meyer et al. 2012; Finke 2013).

In the first stage, we preliminary constrain the parameter space,

² <https://tools.ssdc.asi.it/SED/>

³ *Fermi* LAT Light Curve Repository (LCR) <https://fermi.gsfc.nasa.gov/ssc/data/access/lat/LightCurveRepository/>

⁴ <https://almascience.eso.org/sc/>

¹ The Eddington ratio is defined as: $\lambda = L_{\text{bol}}/L_{\text{Edd}}$, where L_{bol} is the bolometric luminosity, and $L_{\text{Edd}} = 1.3 \times 10^{38} M_{\text{BH}}/M_{\odot}$.

using the phenomenological constraining modules implemented in JetSeT. In the second stage, the minimization of the model was obtained using the JetSeT ModelMinimizer module, plugged to `iminuit` python interface (Dembinski et al. 2023). Finally, we employ a Markov Chain Monte Carlo sampling, to estimate the posterior distribution of the physical parameters of the sources, and of the jet energetic, using the JetSeT McmcSampler module, plugged into the `emcee` sampler (Foreman-Mackey et al. 2013).

In the following section, we describe the details of the SSC/EC model and the relevance of the physical parameters.

4.1 Model description

The model assumes a homogeneous emission region with a spherical shape, located at a distance R_{diss} from the central BH of mass M_{BH} . The emitting region travels along the jet axis with a bulk Lorentz factor Γ , with a viewing angle θ , implying a beaming factor $\delta = 1/(\Gamma(1 - \beta \cos \theta))$. Assuming that the jet has a conical shape, with a semi-opening angle represented by ψ , we introduce the relationship⁵ between the size of the emitting region R and R_{diss} , expressing it as $R = R_{\text{diss}} \tan \psi$.

Since cooling effects primarily influence the SED of the sources, we model them by assuming that the emitting region is filled with electrons following a broken power-law energy distribution, given by:

$$N(\gamma) \propto \begin{cases} \gamma^{-p} & \gamma_{\text{min}} \leq \gamma < \gamma_{\text{b}} \\ \gamma^{-p_1} & \gamma_{\text{b}} \leq \gamma \leq \gamma_{\text{max}}, \end{cases} \quad (1)$$

with the number density of the electrons

$$N_e = \int_{\gamma_{\text{min}}}^{\gamma_{\text{max}}} N(\gamma) d\gamma, \quad (2)$$

where, γ_{min} , γ_{b} and γ_{max} are the minimum, break, and maximum electron Lorentz factor, respectively, and p and p_1 the low-energy and high-energy spectral index. The relativistic electrons interact with the entangled magnetic field, B , emitting synchrotron and inverse Compton radiation (IC). For the IC, the full Compton cross-section for relativistic electrons including the Klein-Nishina regime is considered.

To reproduce the beaming pattern of the EC emission (Dermer 1995), we use the disk external field transformation in JetSeT, which follows the approach of Georganopoulos et al. (2001), ensuring the correct dependence of the beaming pattern on the observing angle.

In cases where an optical-UV excess flux is observed in the SED, we can estimate the accretion disk physical parameters and set the black hole mass. On the other hand, in cases where the jet emission dominates, the values of M_{BH} are taken from the literature, mainly derived from spectroscopy, through the luminosity of the broad emission lines, (see e.g., Berton et al. 2021).

We assume that the accretion disk extends from, $R_{\text{in}} = 3R_{\text{S}}$, to $R_{\text{out}} = 500R_{\text{S}}$ (R_{S} is the Schwarzschild radius, $R_{\text{S}} = 2GM_{\text{BH}}/c^2$) with an emission profile that has a multi-temperature blackbody shape (Frank et al. 2002; Ghisellini & Tavecchio 2009). The radial dependence of the temperature is given by:

$$T(R) = \left\{ \frac{3R_{\text{S}}L_{\text{Disk}}}{16\pi\eta\sigma R^3} \left[1 - \left(\frac{R_{\text{in}}}{R} \right)^{1/2} \right] \right\}^{1/4}, \quad (3)$$

⁵ Following the JetSeT documentation

where σ is the Stefan-Boltzmann constant, and η is the accretion efficiency linked to the accretion rate \dot{M} , and to the bolometric luminosity. Assuming that $L_{\text{bol}} \propto L_{\text{Disk}}$, the disk luminosity is given by $L_{\text{Disk}} = \eta\dot{M}c^2$. We have not considered the disk corona emission.

The BLR is assumed to be a spherical thin shell with a radius that scales with the disk luminosity following the relation⁶,

$$R_{\text{BLR}} = 3 \times 10^{17} (L_{\text{Disk},46})^{1/2} \text{ cm}, \quad (4)$$

given by Kaspi et al. (2007). The DT is modeled as a black body with temperature T_{DT} , constrained from ~ 100 K up to dust sublimation temperature ~ 2000 K⁷ (Ghisellini & Tavecchio 2008, 2009). Its radius is estimated using the relation by Błażejowski et al. (2000),

$$R_{\text{DT}} = 2.5 \times 10^{18} (L_{\text{Disk},45})^{1/2} \text{ cm}. \quad (5)$$

We assume a fraction $\tau_{\text{BLR}} = 0.1$ of L_{Disk} is reprocessed by the BLR, and a fraction $\tau_{\text{DT}} = 0.1-0.3$ by the DT Ghisellini & Tavecchio (2009). The effect of extragalactic background light absorption was taken into account (Franceschini et al. 2008).

4.1.1 Jet power

We get the energetic content of the jet obtained from the SED modeling and the jet power carried by electrons (P_e), Poynting flux (P_B), radiation (P_{rad}), and cold protons (P_p) as follows (Celotti & Ghisellini 2008):

$$P_i = \pi R^2 \beta c \Gamma^2 U'_i, \quad (6)$$

where R is the size of the emission region, βc is the plasma velocity, and U'_i is the comoving energy density of relativistic electrons ($i=e$), magnetic field ($i=B$), radiation ($i=rad$), and cold protons ($i=p$). The single-sided jet power is given by:

$$P_{\text{jet}} = \pi R^2 \beta c \Gamma^2 (U'_e + U'_B + U'_p + U'_r), \quad (7)$$

and we have assumed one proton per electron to estimate the cold protons energy density.

The derived parameters of the modeling are displayed in Tables 1, 2, and 3. The best fits obtained by MCMC are shown as posterior contour maps for the relevant parameters of each model in Figures A1, A2 and A3, as well as a comparison of the derived jet power posterior distribution with a sample of γ -NLS1 and FSRQ in Figures 2, 4 and 6.

5 RESULTS

We have modeled the average SED of the three sources to derive the physical parameters associated with the accretion disk, the jet, and the surrounding photon environment. In this section, we present the results derived from the fit of the SED using JetSeT.

5.1 PKS 2004-447

To determine whether the physical characteristics of the γ -ray emitter PKS 2004-447 confirm its hybrid nature (NLS1/CSS), we examined the following models. Motivated by the hypothesis that NLS1 galaxies can be considered as CSS viewed at small angles, we model the

⁶ $L_{\text{Disk},X}$ is defined as the disk luminosity in 10^X erg s^{-1} units.

⁷ Sublimation temperature of graphite dust grains (García-González et al. 2017)

SED for different viewing angles (e.g. Oshlack et al. 2001; Komossa et al. 2006; Berton et al. 2016).

Previous studies modeled the SED of PKS 2004-447 assuming the jet is oriented very close to the line of sight, as expected for γ -NLS1 sources ($\theta = 2^\circ$ and 3° , see e.g., Paliya et al. 2013; Gokus et al. 2021). Also, different authors have found that the jet of PKS 2004-447 may have a non-negligible inclination, similar to what is expected for CSS. Particularly, Schulz et al. (2016) estimate an upper limit of $\theta < 50^\circ$ based on radio maps. Therefore, in addition to modeling the SED with a small viewing angle of $\theta = 2^\circ$, we have investigated a scenario where the jet is oriented at a larger viewing angle, assuming an upper limit around $\theta = 15^\circ$ (larger angles result in a notable reduction in gamma-ray emission, attributed to the angle dependence in the Compton-scattering processes, see e.g., Georganopoulos et al. 2001; Finke 2016).

The best model obtained to fit the multi-wavelength data collected for PKS 2004-447 is shown in Figure 1. As we can observe, the low-energy hump is dominated by the jet emission, and the big blue bump produced by the accretion disk is not visible. In this case, to estimate L_{Disk} , we constrained this parameter within a range going from $(1 \times 10^{42} - 4 \times 10^{44}) \text{ erg s}^{-1}$, based on the values reported by different authors on this source (Oriente et al. 2015; Foschini et al. 2017; Berton et al. 2021). Since in the literature, low M_{BH} values have been used for modeling the broadband SED of PKS 2004-447, we have taken a different approach using a larger value of the M_{BH} , i.e. $M_{\text{BH}} = 6 \times 10^8 M_\odot$ estimated by Baldi et al. (2016). Additionally, we examined a case with a lower value derived from the optical spectrum, $M_{\text{BH}} = 1.5 \times 10^7 M_\odot$ (Berton et al. 2021). For each BH mass value, we present two models: one scenario with $\theta = 2$ and another testing a larger viewing angle.

To explore the size of the blob and its distance from the BH, we have set the opening angle of the jet as a free parameter, constrained by a maximum value of 5.72° , as is usually assumed for blazars (Ghisellini & Tavecchio 2009). The opening angle and the blob size derived from the fit, allow us to calculate the Doppler factor δ and variability timescale $\Delta\tau_v$, reported in Table 1. In addition, we have computed the Eddington luminosity and the Eddington ratio. The parameters obtained with the best-fit models are presented in Table 1.

5.1.1 Models assuming high black hole mass

Within the framework of the jet oriented at $\theta = 2^\circ$, adopting a $M_{\text{BH}} = 6 \times 10^8 M_\odot$ Baldi et al. (2016), we have derived a $L_{\text{Disk}} = 1.33 \times 10^{43} \text{ erg s}^{-1}$ (it is important to be cautious with this luminosity value obtained from the fit, since the optical/UV spectrum does not allow direct observation of the accretion disk emission). In this model, the first hump of the SED from IR to UV data is well reproduced assuming synchrotron emission, and the second hump at high energies is mainly dominated by the EC process generated by the dusty torus photon field. We derived a magnetic field strength of $B = 0.53 \text{ G}$, and a Bulk Lorentz factor of $\Gamma = 10.07$. The emitting region is located outside the BLR but inside the dusty torus.

In the second scenario, we tested a jet oriented with a viewing angle larger than 2 degrees, and θ set as a free parameter constrained by an upper limit of $\theta = 15^\circ$. We also set as free parameters the magnetic field and the parameters associated with the electron distribution to fit the SED. We obtained from the best fit a $\theta = 9.5^\circ$, with a statistic $\chi_r^2 = 1.99$. In contrast to the model with $\theta = 2^\circ$, the X-ray and γ -ray data are explained by SSC emission, and the low-frequency radio data are well reproduced by the synchrotron emission. We derived a low Bulk Lorentz factor $\Gamma = 4.37$, and a low magnetic field $B = 0.018 \text{ G}$,

Table 1. Column (1): Parameter name. Column (2): Model of PKS 2004-447 assuming a viewing angle of $\theta = 2^\circ$ and M_{BH} taken from (Baldi et al. 2016). Column (3): Same as Column 2, but with a larger viewing angle. Column (4): Model of PKS 2004-447 assuming a viewing angle of $\theta = 2^\circ$ and M_{BH} taken from (Berton et al. 2021). Column (5): Same as Column 4, but with a larger viewing angle.

Parameter	PKS 2004-447				
	(1)	(2)	(3)	(4)	(5)
p	2.10	1.96	2.16	1.96	1.96
p _l	3.98	2.38	4.12	2.29	2.29
γ'_{min}	26.51	53.74	15.57	60.13	60.13
γ'_{b}	1.5×10^3	1.27×10^3	1.42×10^3	526.4	526.4
γ'_{max}	1.32×10^4	3.81×10^4	1.33×10^4	4.01×10^4	4.01×10^4
$N [\text{cm}^{-3}]$	4.76×10^3	8.97	7.04×10^3	5.74	5.74
$B [\text{G}]$	0.53	0.018	0.62	0.014	0.014
Γ	10.07	4.37	10.0	4.20	4.20
$R_{\text{diss}} [\text{cm}]$	4.73×10^{16}	5.77×10^{18}	5.73×10^{16}	9.75×10^{18}	9.75×10^{18}
$R_{\text{blob}} [\text{cm}]$	3.44×10^{15}	4.77×10^{17}	3.82×10^{15}	7.09×10^{17}	7.09×10^{17}
$\Psi [\text{deg}]$	4.12	4.69	3.37	4.12	4.12
$\theta [\text{deg}]$	2.0^f	9.5	2.0^f	10.8	10.8
$M_{\text{BH}} [M_\odot]$	6×10^{8f}	6×10^{8f}	1.5×10^{7f}	1.5×10^{7f}	1.5×10^{7f}
$L_{\text{Disk}} [\text{erg s}^{-1}]$	1.33×10^{43}	5×10^{42}	2.53×10^{43}	4×10^{43}	4×10^{43}
η	0.08^f	0.08^f	0.08^f	0.08^f	0.08^f
$R_{\text{DT}}^f [\text{cm}]$	2.89×10^{17}	1.76×10^{17}	3.97×10^{17}	5×10^{17}	5×10^{17}
$T_{\text{DT}} [\text{K}]$	170	230	299	208	208
τ_{DT}	0.3^f	0.3^f	0.3^f	0.3^f	0.3^f
τ_{BLR}	0.1^f	0.1^f	0.1^f	0.1^f	0.1^f
$R_{\text{BLR, in}}^f [\text{cm}]$	1.15×10^{16}	7.07×10^{15}	1.59×10^{16}	2×10^{16}	2×10^{16}
$R_{\text{BLR, out}}^f [\text{cm}]$	1.27×10^{16}	7.77×10^{15}	1.75×10^{16}	2.2×10^{16}	2.2×10^{16}
$P_e [\text{erg s}^{-1}]$	43.67	44.92	43.68	45.04	45.04
$P_B [\text{erg s}^{-1}]$	42.11	42.71	42.32	42.84	42.84
$P_r [\text{erg s}^{-1}]$	42.12	43.34	42.08	43.47	43.47
$P_p [\text{erg s}^{-1}]$	44.90	45.73	45.16	45.84	45.84
$P_{\text{tot}} [\text{erg s}^{-1}]$	44.93	45.79	45.17	45.91	45.91
$U'_e [\text{erg s}^{-3}]$	4.13×10^{-1}	2.11×10^{-3}	3.56×10^{-1}	1.36×10^{-3}	1.36×10^{-3}
$U'_B [\text{erg s}^{-3}]$	1.15×10^{-2}	1.29×10^{-5}	1.53×10^{-2}	8.61×10^{-6}	8.61×10^{-6}
$L_{\text{Edd}} [\text{erg s}^{-1}]$	7.8×10^{46}	7.8×10^{46}	1.95×10^{45}	1.95×10^{45}	1.95×10^{45}
λ_{Edd}	1.7×10^{-4}	6.4×10^{-5}	0.012	0.02	0.02
δ	17.89	4.63	17.79	4.89	4.89
$\Delta\tau_v [\text{days}]$	0.09	49.31	0.10	69.44	69.44
$\chi_r^2/\text{d.o.f}$	1.82/12	1.99/13	1.71/12	1.19/13	1.19/13

^f Fixed parameters during the fit

required to reproduce the γ -ray emission. The size of the emitting region is estimated of $R_{\text{blob}} = 4.77 \times 10^{17} \text{ cm}$, located at a distance $R_{\text{diss}} = 5.77 \times 10^{18} \text{ cm}$ from the BH, beyond the DT radius.

5.1.2 Models assuming low black hole mass

When we assume a black hole mass of $M_{\text{BH}} = 1.5 \times 10^7 M_\odot$ (Berton et al. 2021), we find that, at an angle of $\theta = 2^\circ$, the parameters derived from the fit are very similar to those obtained with the model assuming a BH mass of $M_{\text{BH}} = 6 \times 10^8 M_\odot$ (Baldi et al. 2016), as we can observe in the Table 1. The low-frequency hump is well explained by synchrotron radiation, and the gamma-ray emission is effectively reproduced by EC emission dominated by seed photons from the dusty torus. Similarly, when we set the viewing angle as a free parameter, the derived parameters resemble those obtained from the model assuming the higher mass; reproducing the SED with an SSC-dominated model but, this time obtaining a $\theta = 10.8^\circ$. The main difference with the models where we assumed a higher black hole mass, lies in the estimated Eddington rate, which depends on the black hole mass and disk luminosity.

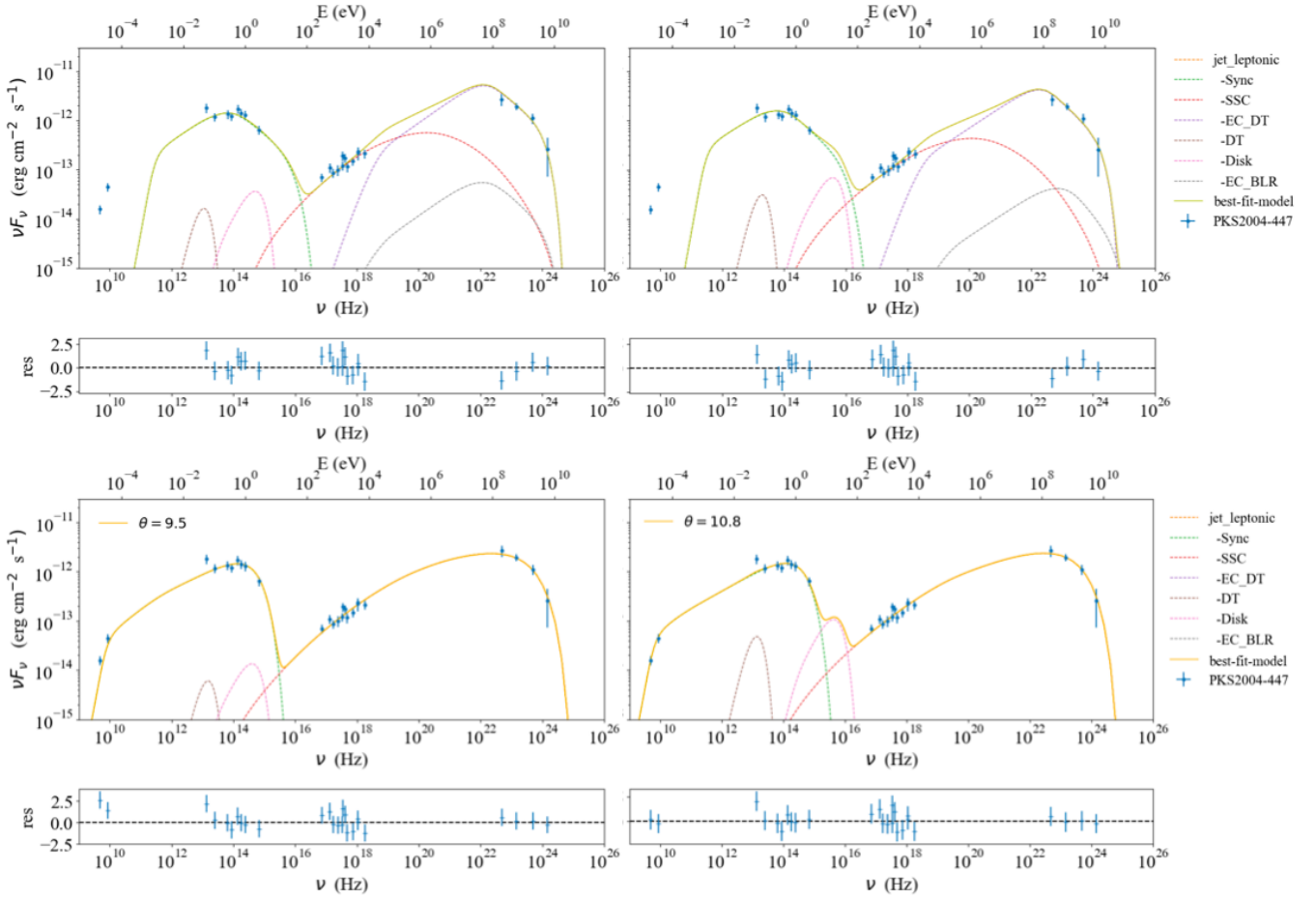


Figure 1. Top left panel: Broadband SED of PKS 2004-447 modeled assuming a viewing angle of $\theta = 2^\circ$ and a $M_{\text{BH}} \sim 6 \times 10^8 M_\odot$ (Baldi et al. 2016). The low-energy hump is reproduced by synchrotron emission, the dusty torus component with a peak at IR frequencies, and the accretion disk component. The high-energy hump is reproduced by a combination of the SSC emission and EC scattering of the BLR and dusty torus photons. The best fit was achieved with a model where the low-energy bump is dominated by synchrotron emission, while the high-energy bump is reproduced by SSC+EC emission, with external Compton dominated by photons coming from the dusty torus. Bottom left panel: The best fit assuming a viewing angle larger than $\theta = 2^\circ$ and the same M_{BH} as in the top panel. From the fit, a jet oriented at $\theta = 9.5^\circ$ was derived. In this case, the high-energy bump is dominated by SSC emission. Top right panel: The best-fit model for the SED of PKS 2004-447 assuming a $M_{\text{BH}} \sim 1.5 \times 10^7 M_\odot$ (Berton et al. 2021), and a viewing angle of $\theta = 2^\circ$. The low-energy hump is dominated by synchrotron emission, and the high-energy hump is dominated by EC scattering of dusty torus photons. Bottom right panel: Model assuming the viewing angle as a free parameter, obtaining $\theta = 10.8^\circ$ from the fit. The high-energy hump is dominated by SSC emission.

5.2 3C 286

To explore the hybrid nature of 3C 286 (CSS/NLS1), we present two models of the SED. These models consider the jet oriented at two different angles. Before conducting the broadband modeling, we determined the black hole mass by fitting the simultaneous optical-UV data using the JetSeT model for the accretion disk, deriving a black hole mass of $M_{\text{BH}} = 3.5 \times 10^8 M_\odot$. We then assumed this value in both models. We have built the radio to γ -rays SED, using the simultaneous optical-UV-X-ray data measured on August 2020, by the *Swift* telescope and published by Yao & Komossa (2021), in addition to the archival data collected from the ASDC SED Builder. The collected SED along with the best fit associated with the models are shown in Figure 3. The parameters derived from the SED fit are reported in Table 2.

5.2.1 Model assuming a small viewing angle

We assumed an observing angle of $\theta = 3^\circ$ as usually adopted for γ -NLS1s (see e.g. Abdo et al. 2009b; Paliya et al. 2019; Gokus et al. 2021), we fixed the black hole mass and set the disk luminosity and accretion efficiency as free parameters. Given the strong emission observed in the SED in the optical/UV bands coming from the accretion disk, we have constrained the range of η to 0.06-0.1 (see e.g., Ghisellini & Tavecchio 2015). This range is consistent with the radiative efficiency of the accretion disk. From the fit, we obtained a disk luminosity of $L_{\text{Disk}} = 6.6 \times 10^{46} \text{ erg s}^{-1}$, and an accretion efficiency of $\eta = 0.072$. The best fit is shown in the top panel of Figure 3, where the low-energy hump, is well reproduced by a combination of synchrotron emission, thermal emission from the dusty torus, and a significant contribution from the accretion disk. For the high-energy hump, we accurately reproduced the X-ray emission with a combination of the emission of the synchrotron high-energy tail, the SSC, and the EC emission from the dusty torus. The best fit

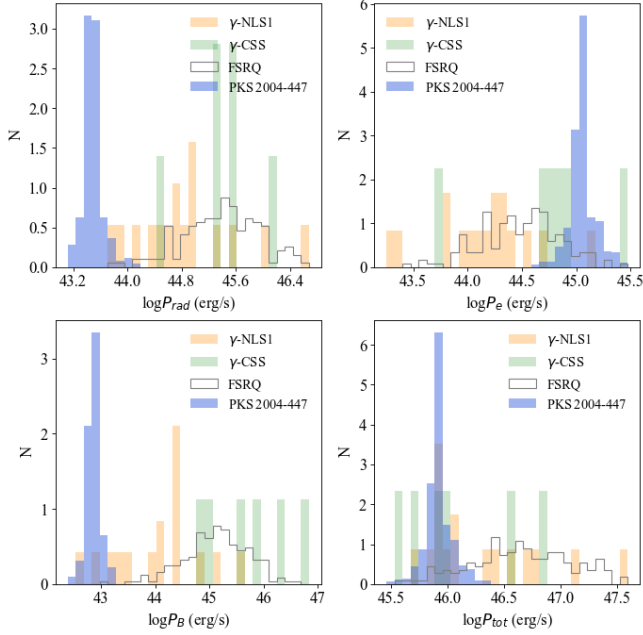


Figure 2. Posterior distribution of jet power components of PKS 2004-447, obtained from the model presented in Column (5) of Table 1, including radiation, electrons, and magnetic content, derived through the MCMC technique. The figure illustrates as a comparison, the jet power components of a sample of FSRQs (grey hatched area), γ -NLS1s (orange shaded area) and γ -CSSs (green shaded area), taken from Ghisellini et al. (2014); Paliya et al. (2019); Zhang et al. (2020), respectively. FSRQs predominantly exhibit a jet dominated by P_{rad} , where $P_p > P_{\text{rad}}$. This translates to matter dominated jets. γ -CSS jets, as characterized by Zhang et al. (2020), display high magnetization and radiation efficiency. γ -NLS1, share a composition similar to that of blazars, with the power of the particles dominating the total jet power.

for the γ -rays came mainly from the EC driven by seed photons from the BLR, with a contribution from the dusty torus seed photons. The dissipation region is located at $R_{\text{diss}} = 5 \times 10^{18}$ cm, outside the BLR but within the dusty torus radius. From the obtained parameters, the Eddington ratio $\lambda_{\text{Edd}} = 1.52$ and the Doppler factor is $\delta = 16.80$.

5.2.2 Misaligned jet model

Assuming that the jet is oriented at a larger viewing angle, consistent with the observed jets in the CSS class, we set θ as a free parameter constrained from 3° to 15° . We used the parameters derived from the model with a small viewing angle as a starting point for the fit. The parameters associated with the accretion disk component: L_{Disk} , M_{BH} , and the accretion efficiency, were fixed. Meanwhile, we set the magnetic field, the bulk Lorentz factor, the size of the emitting region, and its distance along the jet as free parameters.

Due to the dependence of EC emission on θ (see e.g., Dermer 1995), we found that it is not possible to fit the SED using a viewing angle larger than $\sim 8^\circ$. As a result, our best fit was found with $\theta = 7.1 \pm 0.3$. The model converges to a dissipation region located at $R_{\text{diss}} = 2.22 \times 10^{19}$ cm ≈ 7.19 pc, an emitting region size $R_{\text{blob}} = 1.77 \times 10^{18}$ cm, and a magnetic field of $B = 0.14$ G. As observed in Figure 3, in this model, the self-absorption frequency, $\nu_{\text{SSA}} \propto \left(\frac{B^2}{2} RN \right)^{\frac{2}{p+4}}$ (see e.g., Ghisellini 2013), is redder than in the model with $\theta = 3^\circ$, allowing us to fit the radio data. The γ -rays are well

Table 2. Column (1): Parameter name. Column (2): Parameters obtained from the SED fit of 3C 286, assuming a viewing angle of 3° . Column (3): Model of 3C 286 for the CSS scenario.

Parameter	3C 286	
(1)	(2)	(3)
p	1.67	2.2
p_l	3.5	3.2
γ'_{min}	30.0	67.1
γ'_b	316.2	456.7
γ'_{max}	8.0×10^4	1.18×10^5
N [cm $^{-3}$]	1.03	0.18
B [G]	0.22	0.14
Γ	11.39	8.31
R_{diss} [cm]	5×10^{18}	2.22×10^{19}
R_{blob} [cm]	4×10^{17}	1.77×10^{18}
Ψ [deg]	4.58^f	4.58^f
θ [deg]	3.0^f	7.1
M_{BH} [M_\odot]	3.5×10^{8f}	3.5×10^{8f}
L_{Disk} [erg s $^{-1}$]	6.6×10^{46}	6.6×10^{46f}
η	0.072	0.069
R_{DT}^f [cm]	5.26×10^{19}	5.13×10^{19}
T_{DT} [K]	100	100
τ_{DT}	0.15^f	0.15^f
τ_{BLR}	0.1^f	0.1^f
$R_{\text{BLR,in}}^m$ [cm]	7.89×10^{17}	7.7×10^{17}
$R_{\text{BLR,out}}^m$ [cm]	8.68×10^{17}	8.47×10^{17}
P_e [erg s $^{-1}$]	44.28	44.74
P_B [erg s $^{-1}$]	45.58	46.22
P_r [erg s $^{-1}$]	43.69	44.71
P_p [erg s $^{-1}$]	45.48	45.75
P_{tot} [erg s $^{-1}$]	45.85	46.37
U'_e [erg s $^{-3}$]	9.9×10^{-5}	2.7×10^{-5}
U'_B [erg s $^{-3}$]	1.95×10^{-3}	8.29×10^{-4}
L_{Edd} [erg s $^{-1}$]	4.55×10^{46}	4.55×10^{46}
λ_{Edd}	1.52	1.45
δ	16.80	8.09
$\Delta \tau_v$ [days]	17.00	156.81
$\chi^2_{\text{r}}/\text{d.o.f}$	1.81/20	0.66/23

^f Fixed parameters during the fit

^m model dependent parameters. $R_{\text{BLR,out}}$ is fixed at $1.1 R_{\text{BLR,in}}$

reproduced with EC emission dominated by seed photons from the dusty torus.

5.3 PKS 0440-00

We have modeled the SED of PKS 0440-00 using parameters typical of FSRQs, in agreement with its initial classification. Two models are presented: one constraining the emission region to be within the BLR and another placing it outside the BLR but within the dusty torus. In both models, we adopt a small viewing angle of $\theta = 3^\circ$ and a jet opening angle of $\Psi = 5.72^\circ$ (see e.g., Ghisellini & Tavecchio 2015). By fitting the optical/UV data, we derived the black hole mass and accretion disk luminosity, obtaining a $M_{\text{BH}} = 1.73 \times 10^8 M_\odot$ and $L_{\text{Disk}} = 1.71 \times 10^{46}$ erg s $^{-1}$. These values were fixed in both models, assuming a radiative efficiency of $\eta = 0.08$ (see e.g., Ghisellini & Tavecchio 2009). To estimate the radius of the dusty torus component, we extended the functional dependency based on the disk luminosity, and discussed in section 4, with the sublimation temperature and the size of the dust grains (Kishimoto et al. 2007), according to:

$$R_{\text{DT}} = 1.3 \left(\frac{L_{\text{UV}}}{10^{46} \text{ erg/s}} \right)^{1/2} \left(\frac{T_{\text{sub}}}{1500 \text{ K}} \right)^{-2.8} \left(\frac{a}{0.05 \mu\text{m}} \right)^{-1/2} \text{ cm}, \quad (8)$$

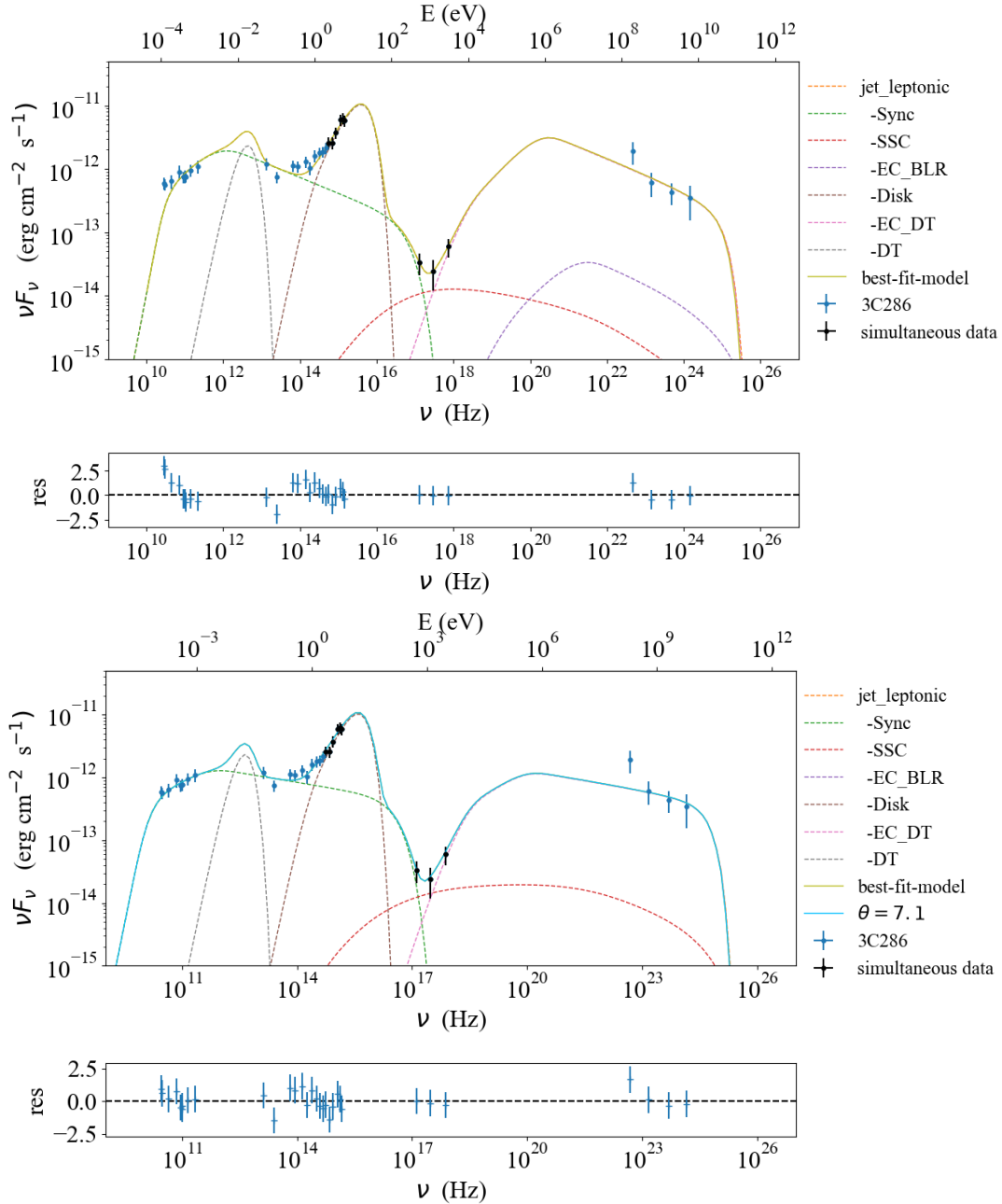


Figure 3. Top panel: Broadband SED and model fit of 3C286 assuming a viewing angle of $\theta = 3^\circ$. The low-energy hump is reproduced by synchrotron emission, a dusty torus component peaking at IR frequencies, and the accretion disk component. The high-energy hump is reproduced by a combination of the SSC emission and EC scattering of the BLR and dusty torus photons. Bottom panel: The best model fit for the CSS scenario; with a derived observing angle of $\theta \approx 7.1^\circ$. The high-energy hump is dominated by the torus-EC emission.

where we assumed that the dust concentration at the radius R_{DT} , is mainly dominated by graphite grains with a size $a = 0.05 \mu\text{m}$ at T_{sub} , which is considered as a free parameter within the range $T_{\text{sub}} = [1000 - 2000] \text{K}$ (see e.g., Błażejowski et al. 2000; Kishimoto et al. 2007). L_{UV} , is defined as the UV-optical luminosity of the central engine, which we have assumed as L_{Disk} . The collected multiwavelength data, along with the best fit models are shown in Figure 5. The parameters obtained with the best-fit models are presented in Table 3.

5.3.1 Model with the emission region located outside the BLR but inside the dusty torus

From the best fit we have found that the emission region is located at a distance of $R_{\text{diss}} = 1.4 \times 10^{18} \text{cm}$ from the BH. In this model (see top panel of Figure 5), we successfully reproduce the low energy hump of the SED with a combination of synchrotron emission and the thermal components from the dusty torus and accretion disk. We found a temperature of the DT of $\sim 1693 \text{K}$. The high energy hump is well reproduced with an SSC+EC emission, where the main

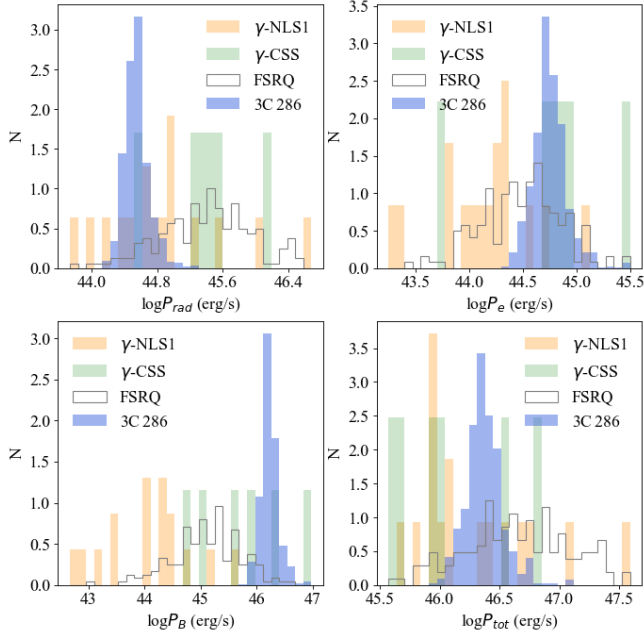


Figure 4. Same as Figure 2, but for the jet power components of 3C 286, obtained from the model presented in Column (3) of Table 2.

contribution to the X-ray emission comes from the SSC. The EC used to fit the gamma-rays is dominated by photons from the DT.

5.3.2 Model with the emission region within the BLR radius

When we assumed that the emission region is located inside the BLR, we found that the model fails to reproduce the radio emission (see bottom panel in Figure 5), and the gamma-rays are noticeably absorbed around 10 GeV energies. To obtain a better fit, we have calculated the optical depth for γ -ray photons and corrected the observed flux for γ - γ absorption. In this model, the dominant component driving gamma-ray emission is the EC produced by seed photons from the BLR. The X-rays are well fitted with an SSC component.

6 DISCUSSION

In this section, we will discuss the physical parameters derived from the models presented in section 5, to understand the hybrid nature of the sources.

6.1 PKS 2004-447

The multiwavelength SED of this source, built with the collected data indicates a blazar-like nature, with the gamma-ray emission confirming the presence of a relativistic jet. In the optical bands, this source is classified as an NLS1, due to its relatively weak [OIII] emission and narrow H β line (Oshlack et al. 2001; Berton et al. 2021). In radio, characteristics such as the steep spectral index ($\alpha < -0.5$, see e.g., Gallo et al. 2006) and core-jet morphology suggest a CSS classification (see e.g., Oshlack et al. 2001; Gallo et al. 2006; Schulz et al. 2016). In addition, flux density measurements display a moderate slow variability in radio ($\sim 20\%$ on the timescale of years) that are commonly found in CSS sources (Edwards & Tingay 2004).

Table 3. Column (1): Parameter symbol. Column (2): Parameters obtained from the SED fit of PKS 0440-00, taking into account the sublimation radius of the dust, assuming graphite grains with a size of $0.05 \mu\text{m}$, for a $T_{\text{DT}} = [1000, 2000]$ K. Column (3): Testing the dissipation region closer to the BLR radius.

Parameter	PKS 0440-00	
(1)	(2)	(3)
p	1.96	1.77
p_1	3.60	2.84
γ'_{min}	7.69	1^f
γ'_b	627.2	200.0
γ'_{max}	8.8×10^4	4.1×10^3
$N [\text{cm}^{-3}]$	146.83	1.18×10^5
$B [\text{G}]$	0.15	1.8
Γ	15.49	11.21
$R_{\text{diss}} [\text{cm}]$	1.4×10^{18}	1×10^{17}
$R_{\text{blob}} [\text{cm}]$	1.4×10^{17}	5×10^{15}
$\Psi [\text{deg}]$	5.72^f	2.86^f
$\theta [\text{deg}]$	3.0^f	3.0^f
$M_{\text{BH}} [M_{\odot}]$	1.73×10^{8f}	1.73×10^{8f}
$L_{\text{Disk}} [\text{erg s}^{-1}]$	1.71×10^{46f}	1.71×10^{46f}
η	0.08^f	0.08^f
$R_{\text{DT}}^f [\text{cm}]$	2.18×10^{19}	1.79×10^{19}
$T_{\text{DT}} [\text{K}]$	1693	1800
$T_{\text{sub}} [\text{K}]$	900	965
τ_{DT}	0.3^f	0.3^f
τ_{BLR}	0.1^f	0.1^f
$R_{\text{BLR, in}}^m [\text{cm}]$	3.93×10^{17}	3.93×10^{17}
$R_{\text{BLR, out}}^m [\text{cm}]$	4.32×10^{17}	4.32×10^{17}
$P_e [\text{erg s}^{-1}]$	45.33	44.44
$P_B [\text{erg s}^{-1}]$	44.62	43.59
$P_r [\text{erg s}^{-1}]$	44.55	44.36
$P_p [\text{erg s}^{-1}]$	46.98	46.72
$P_{\text{tot}} [\text{erg s}^{-1}]$	47.00	46.73
$U'_e [\text{erg s}^{-3}]$	4.89×10^{-3}	9.34×10^{-1}
$U'_B [\text{erg s}^{-3}]$	9.60×10^{-3}	1.3×10^{-1}
$L_{\text{Edd}} [\text{erg s}^{-1}]$	2.25×10^{46}	2.25×10^{46}
λ_{Edd}	0.76	0.76
δ	18.69	16.66
$\Delta\tau_v [\text{days}]$	5.33	0.21
$\chi_r^2/\text{d.o.f}$	0.86/13	4.56/12

^f Fixed parameters during the fit

^m model dependent parameters. $R_{\text{BLR, out}}$ is fixed at $1.1 R_{\text{BLR, in}}$

Our best model shows that the low-energy hump is dominated by jet emission, i.e. synchrotron radiation. This is also the case when modeling different activity states, a result recently reported by Gokus et al. (2021). On the other hand, the high-energy hump, as seen in Figure 1, can be reproduced by either an SSC-dominated model or a combination of SSC+EC processes, depending on the orientation of the jet.

We obtain from the best fit of all the models, a relatively low $L_{\text{Disk}} \sim 10^{43} \text{erg s}^{-1}$ that is in agreement with recent work by Gokus et al. (2021). Since the SED is dominated by jet emission, it is not possible to disentangle the contribution of the disk from that of the jet, therefore we might be underestimating the true luminosity of the disk. However, we found that values close to or above $\sim 10^{44} \text{erg s}^{-1}$, overestimate the SED flux in the optical/UV bands.

6.1.1 The jet orientation

Adopting a small viewing angle ($\theta = 2^\circ$), our best fit was obtained with an SSC+EC model, where the gamma-rays are dominated by

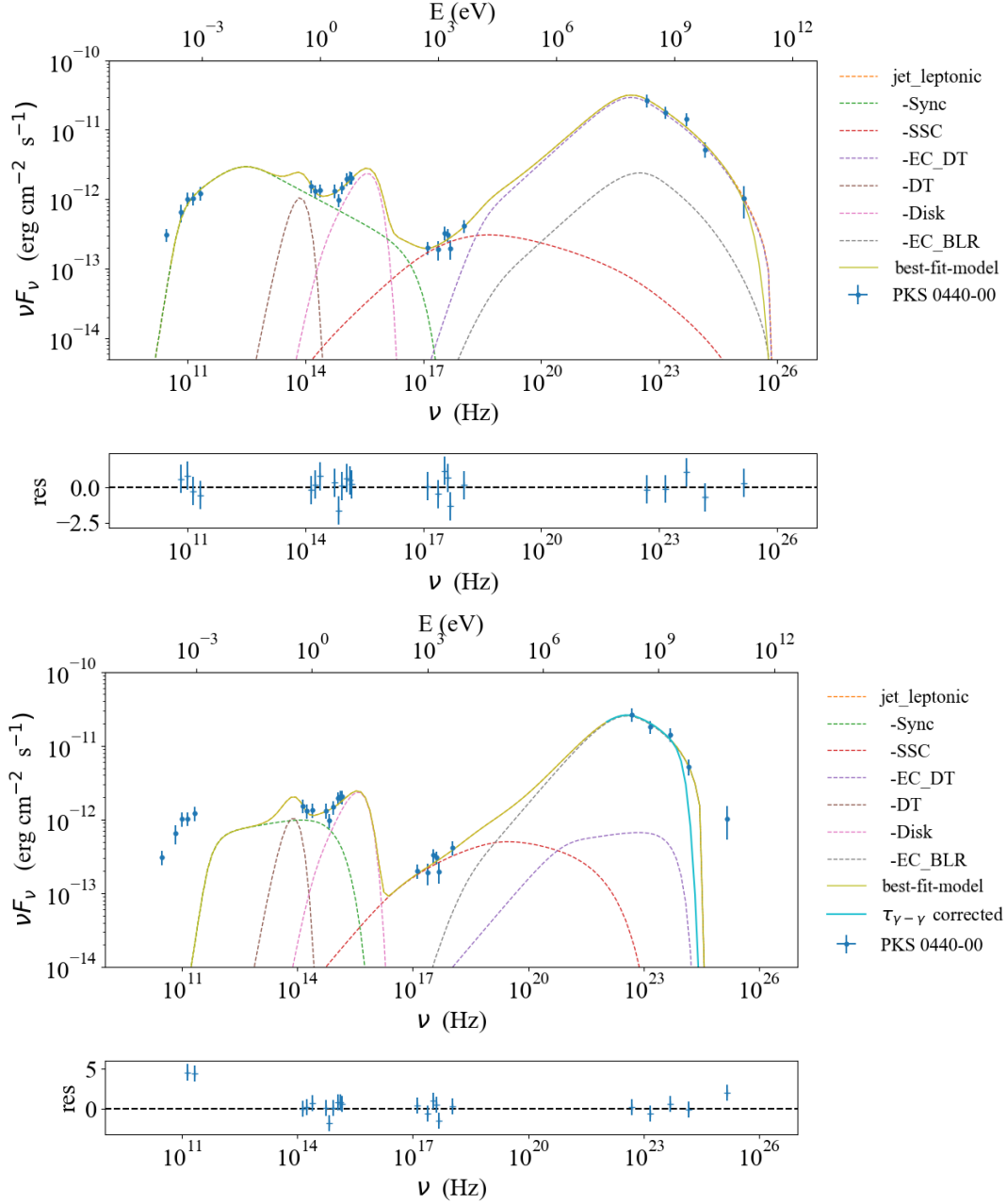


Figure 5. Top panel: Modeled broadband SED of PKS 0440-00 assuming a dusty torus radius scaling following equation 8. Bottom panel: Model of the SED of PKS 0440-00 assuming the dissipation region located inside the BLR. In blue the γ -ray emission is corrected by the $\gamma - \gamma$ absorption.

the EC emission produced by the DT (see top panels of Figure 1). Similar results have been found also by other studies (see e.g., Paliya et al. 2019; Gokus et al. 2021). On the other hand, when modeling the SED with a free viewing angle, yielding an angle around 10° , both X-rays and gamma-rays are well reproduced by SSC emission (see bottom panel of Figure 1). Given the observed short timescale variations in gamma-rays from hours to weeks, as noted by Gokus et al. (2021), the smaller viewing angle appears to be a more reliable estimate for this object. However, radio band observations suggest the possibility of a larger angle ($\theta \lesssim 50^\circ$), as reported by Schulz et al. (2016) based on their radio maps. Therefore, our estimated viewing angle of $\sim 10^\circ$ remains valid (it is worth mentioning that it is important the scale at which this angle is estimated since the jet

can undergo orientation changes). Moreover, this value is consistent with those found for γ -CSS sources (Zhang et al. 2020).

6.1.2 Black hole mass and accretion regime

For modeling the SED, two different black hole masses were assumed. From Berton et al. (2021), a black hole mass of $1.5 \times 10^7 M_\odot$ was considered since its estimation seems to be less contaminated by the jet emission. On the other hand, we also used a second value of $6 \times 10^8 M_\odot$ estimated by Baldi et al. (2016). These authors have proposed a higher estimated value, which may be more reliable. They suggest that the BLR clouds could be constrained within a rotating

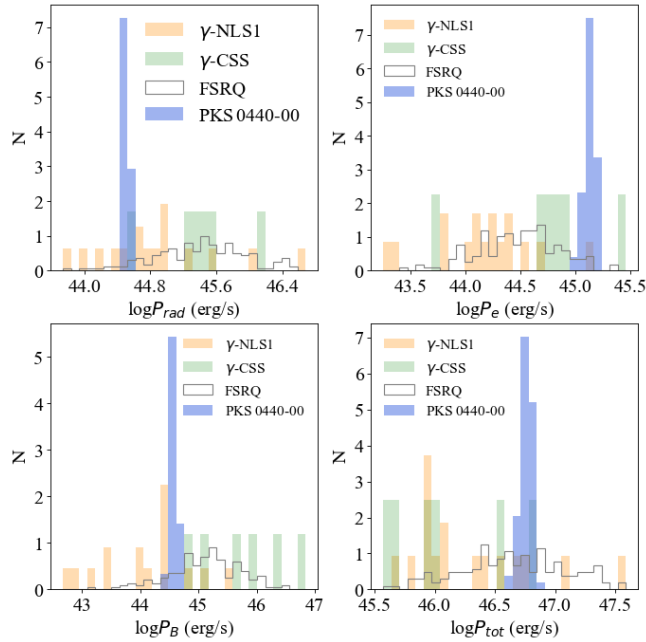


Figure 6. Same as Figure 2, but for the jet power components of PKS 0440-00, obtained from the model presented in Column (2) of Table 3.

disk, potentially leading to a narrower FWHM of the spectral lines. As a result, this could lead to lower estimated black hole masses.

Different black hole masses have an impact on the accretion rate in Eddington units ($\lambda_{\text{Edd}} = L_{\text{bol}}/L_{\text{Edd}}$). We have found that depending on the adopted BH mass and the L_{bol} , the accretion could change from an efficient to an inefficient regime (see Table 4).

To establish the accretion regime for the four models, we first assume L_{Disk} as a proxy of L_{bol} . With this approximation, we have found that the models assuming $6 \times 10^8 M_{\odot}$ indicate an inefficient accretion regime (the transition between efficient to inefficient accretion mode occurs when $\lambda_{\text{Edd,Disk}} \sim 0.01$, Ghisellini 2010a), while assuming $1.5 \times 10^7 M_{\odot}$ suggests an efficient mode. A second approach was done considering now the L_{BLR} , as a tracer of accretion (see e.g., Sbarrato et al. 2014).

When considering L_{BLR} , as a proxy of L_{Disk} , based on the broad emission lines, the transition between efficient and inefficient regime is defined $\lambda_{\text{Edd,BLR}} \sim 5 \times 10^{-4}$ (Sbarrato et al. 2014). Under the accretion falls in the inefficient regime when we adopt a BH mass of $M_{\text{BH}} = 6 \times 10^8 M_{\odot}$, while with $M_{\text{BH}} = 1.5 \times 10^7 M_{\odot}$, the accretion disk becomes efficient. Given that the SED of this source is dominated by jet emission, with no prominent emission from the accretion disk, it is likely that considering L_{Disk} as an approximation of L_{bol} may not be the most appropriate assumption for this source.

Typically, the accretion disk in jetted NLS1 sources is considered to be efficient (see e.g., Abdo et al. 2009b). Thus, assuming a mass of $1.5 \times 10^7 M_{\odot}$, the source seems more consistent with the NLS1 class. However, assuming a BH mass of $M_{\text{BH}} = 6 \times 10^8 M_{\odot}$, we found that the disk is accreting inefficiently. In this case, the accretion will be better described by an advection-dominated accretion flow model (ADAF, see e.g., Narayan et al. 1998, and references therein). According to Chen et al. (2022), an ADAF-type model is the most suitable for this source, providing support for this particular scenario. Having a low accretion rate and a radiatively inefficient disk would naturally explain the relatively low luminosity of the disk.

Table 4. Parameters calculated from the models of PKS 2004-447, with the corresponding black hole mass and viewing angle. R_{BLR} is assumed as $R_{\text{BLR,out}}$, derived from the fit and reported in Table 1. $L_{\text{BLR}} = 4\pi c R_{\text{BLR}}^2 U_{\text{BLR}}$ where U_{BLR} is measured at the disk rest frame, provided by JetSeT. \dot{m} was estimated as $\dot{m} = \dot{M}/M_{\text{Edd}}$, where $\dot{M} = \frac{L_{\text{Disk}}}{\eta c^2}$ and $M_{\text{Edd}} = \frac{L_{\text{Edd}}}{c^2}$.

(1)	$M_{\text{BH}} = 6 \times 10^8 M_{\odot}$		$M_{\text{BH}} = 1.5 \times 10^7 M_{\odot}$	
	$\theta = 2^\circ$	$\theta = 9.5^\circ$	$\theta = 2^\circ$	$\theta = 10.8^\circ$
R_{BLR} [cm]	1.27×10^{16}	7.77×10^{15}	1.75×10^{16}	2.19×10^{16}
U_{BLR} [erg cm $^{-3}$]	2.66×10^{-2}	3.13×10^{-2}	2.55×10^{-2}	2.48×10^{-2}
L_{BLR} [erg s $^{-1}$]	1.62×10^{42}	7.13×10^{41}	2.94×10^{42}	4.5×10^{42}
L_{Disk} [erg s $^{-1}$]	1.33×10^{43}	5×10^{42}	2.53×10^{43}	4×10^{43}
$L_{\text{Edd,Disk}}$ [erg s $^{-1}$]	7.8×10^{46}	7.8×10^{46}	1.95×10^{45}	1.95×10^{45}
$\lambda_{\text{Edd,Disk}}$	1.7×10^{-4}	6.4×10^{-5}	0.012	0.02
$\lambda_{\text{Edd,BLR}}$	2.07×10^{-5}	9.1×10^{-6}	0.001	0.002
\dot{m}	0.002	0.004	0.16	0.25

Low Eddington ratio sources are characterized by weak or no Fe II emissions, as is the case of this source (see e.g., Berton et al. 2021). However, it does exhibit intense oxygen and Balmer emission lines in the optical, characteristic of the NLS1 class, indicating that the accretion disk is producing enough ionizing luminosity. As found by Ghisellini et al. (2011), even BL Lacs, that are low accretion sources can show strong broad emission lines depending on the jet activity state (Sbarrato et al. 2014). The shape of the SED indicates that the jet dominates the emission, hiding the thermal emission from the accretion disk, a characteristic of the BL Lac class. It would be important to consider that this object could be in a transition phase where the accretion is low and the emission lines are the remnants of a previous more active state, i.e. an efficient accretion disk. Based on the above results of the SED modeling, we could support the hybrid nature of the source.

6.1.3 Jet power

The jet power, computed from SED modeling, regardless of the BH mass, exhibits variations depending on the jet orientation and the size of the emitting region (see Table 1). When the jet is oriented at $\theta = 2^\circ$, with dissipation occurring close to the BH and with a strong magnetic field, we found that $P_r \approx P_B$ for the model with $M_{\text{BH}} = 6 \times 10^8 M_{\odot}$, and $P_B > P_r$ when $M_{\text{BH}} = 1.5 \times 10^7 M_{\odot}$.

On the other hand, for the models with a larger θ , the dissipation region is located at larger distances, well beyond the DT. As a consequence, the magnetic field is weaker, resulting in a lower magnetic jet power $P_r > P_B$.

In all models, the power carried by electrons and cold protons dominates the total jet power. This dominance implies a highly efficient conversion of magnetic energy into kinetic energy of the particles, with a part of the magnetic energy preserved as Poynting flux. Interestingly, this is a characteristic observed in AGNs fueled by inefficient accretion modes or ADAFs. In such cases, these sources predominantly emit their energy in kinetic form through radio jets powered via the Bondi mechanism (e.g., Narayan & Yi 1995; Merloni & Heinz 2007; Hardcastle et al. 2007, it is worth mentioning that they consider sub-Eddington accreting SMBHs and low excitation radio galaxies (LERGs) sources). These results suggest that the presence of an inefficient disk in this source is plausible. Furthermore, ADAFs are also observed to be associated with jets that display evidence of interaction with the large-scale environment (Schulz et al. 2016). The emission observed in the radio maps of this source, shows a potential

interaction between the jet and the surrounding medium, a characteristic observed in some CSS sources (e.g., O’Dea 1998; O’Dea & Saikia 2021). Consequently, we can infer that the low accretion mode scenario may point to the hybrid nature of the source.

In Figure 2 we show the posterior distribution of the jet power components derived from the MCMC fit, compared to values reported in the literature for a sample of γ -NLS1, γ -CSS, and FSRQ (for the MCMC plot see Appendix A1).

6.2 3C 286

This source is one of the few CSS detected in γ -rays up to date, and one of the 5 listed in the 4FGL Abdollahi et al. (2020). Peacock & Wall (1982) categorized it for the first time as a CSS, and later, Berton et al. (2017) identified it as a NLS1 due to its optical spectrum features. As a CSS, it exhibits a compact morphology typical of the class, with a core-jet structure visible on pc scales. Based on its apparent proper-motion speed measured from radio maps, an upper limit of 48° for the inclination angle of its jet has been estimated (An et al. 2017, and references therein). The jet structure observed in the radio maps corresponds to a projected linear size of 910 pc, and around 600 pc the jet is seen to bend (An et al. 2017). Therefore, it is crucial to consider the scale at which the angle of inclination of the jet is estimated since it could bend at different scales. Employing a one-zone model, we cannot reproduce both radio emission and gamma-rays at angles close to 48° , primarily due to the dependence of inverse Compton emission on the jet orientation angle (see e.g., Finke 2016). From our results, in Figure 3, we can observe a significant difference in the radio band between the two models. With a viewing angle of $\theta = 3^\circ$ and the emitting region at ≈ 1.6 pc, we observe self-absorption of the synchrotron emission around 10^{11} Hz, with the lower frequencies not accurately reproduced. Meanwhile, with $\theta \sim 7^\circ$ and the emitting region at ≈ 7.19 pc, the model effectively reproduces all radio emissions, providing a better description of the entire SED. The bulk Lorentz factor in both models was found to be 11.39 and 10.36, larger than those of γ -CSS (between 2.4 and 5.5, Zhang et al. 2020) and more consistent with values of γ -NLS1 (10.8 ± 2.4). The low values of bulk Lorentz factor reported in Zhang et al. (2020) are associated with larger viewing angles. It is important to mention that Zhang et al. (2020) employ a two-zone model, estimating larger viewing angles ($\theta = 12.7^\circ$ for 3C 286). However, they still differ from estimates based on radio maps. This suggests that the gamma-ray emission necessarily originates from a region of the jet oriented at a relatively small viewing angle.

6.2.1 Jet power

We have found that in both models the jet power of this source is magnetically dominated, i.e., $P_B > P_r$ and $P_B > P_e$. In Figure 4, we present the posterior distribution of the jet power and its different components, derived from the MCMC fit for the CSS scenario (see top panel of Figure 4), in comparison with the jet power distribution of a sample of γ -NLS1, γ -CSS, and FSRQ (taken from Ghisellini et al. 2014; Paliya et al. 2019; Zhang et al. 2020, respectively). As observed, the derived magnetic power falls within the range of the γ -CSS ($5.98 \times 10^{44} - 6.91 \times 10^{46} \text{ erg s}^{-1}$, Zhang et al. 2020), while the radiation power resembles that of the NLS1 class, falling within the lower end of the distribution ($5.49 \times 10^{43} - 4.78 \times 10^{46} \text{ erg s}^{-1}$, see, Paliya et al. 2019). We notice that a jet highly magnetized was found for the γ -CSS by Zhang et al. (2020). Typically, for powerful blazars like FSRQs, where the luminosity is predominantly in the

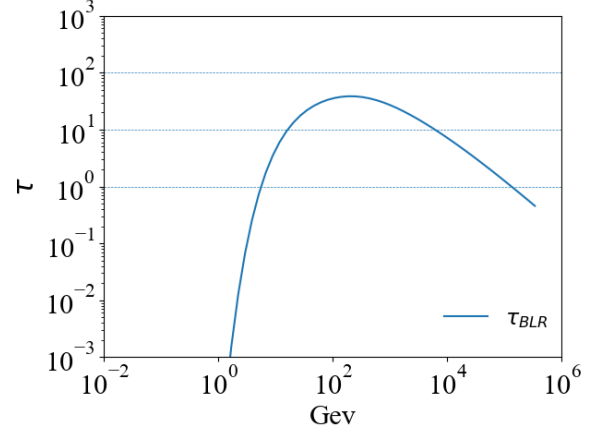


Figure 7. Optical depth as a function of γ -ray photon energy, for the PKS 0440-00 model, where the emitting region is located within the BLR radius.

high energy component, interpreted as EC, the P_B is never dominating. Paliya et al. (2019) have found a similar behavior for the γ -NLS1s sample, also finding a radiative power, P_r to be more than an order of magnitude lower than that derived for blazars studied in Paliya et al. (2017). With a one-zone model, we have obtained an accretion disk luminosity and a magnetically dominated jet, consistent with the results obtained by Zhang et al. (2020).

6.3 PKS 0440-00

In this study, we have presented two different approaches for modeling the broadband SED of PKS 0440-00, to find the best model for reproducing its broadband emission and investigate whether the derived parameters can support the NLS1 classification proposed by Foschini et al. (2021). In the first scenario, we have successfully modeled the SED from radio to gamma-rays using an SSC+EC model with the emitting region located outside the BLR but inside the DT. When considering equation 8 to estimate R_{DT} , even when it implies an oversimplification of the dusty torus component, it provides a good description of the emission by incorporating the composition and size of the dust grains, reproducing the broadband SED with a statistic of $\chi^2 = 0.86$.

The second model (see bottom panel of Figure 5), when the dissipation region is located within the BLR, is disfavored due to the tension with radio data under the synchrotron self-absorption frequency. Additionally, there is a significant pair production within the BLR, due to the interaction between photons produced by broad lines and the blob γ -ray emission (see e.g., Poutanen & Stern 2010), producing a significant γ -ray absorption above 10 GeV (see Figure 7, for the plot of the optical depth for pair production). As a consequence, we conclude that placing the emitting region outside the BLR but inside the DT, provides a better description of the observed emission.

6.3.1 PKS 0440-00 FSRQ or NLS1?

Foschini et al. (2021) pointed out that the optical spectrum of this source shows an H β line with a FWHM $< 2000 \text{ km s}^{-1}$ (Shaw et al. 2012), suggesting a NLS1 classification. This finding is relevant since it is well-known that NLS1s and FSRQs present similar characteristics. Particularly, the broadband SED of γ -NLS1 and FSRQ

show: a steep spectrum in gamma-rays, prominent accretion disk emission in the optical-UV range, a Compton-dominated SED, and synchrotron emission peaking at radio to sub-mm wavelengths (indicative of Low Synchrotron Peak sources, LSP). These characteristics suggest a comparable environment around the jet for both types. Consequently, distinguishing the nature of PKS 0440-447 based on the SED modeling is not straightforward.

We derived a black hole mass of $M_{\text{BH}} = 1.73 \times 10^8 M_{\odot}$ that falls within the distribution values estimated for γ -NLS1 (5×10^6 - $7 \times 10^8 M_{\odot}$, Paliya et al. 2019). The bulk Lorentz factor of $\Gamma = 15.49$, falling within the estimated values for γ -NLS1 and FSRQ, according to Paliya et al. (2019) and Ghisellini & Tavecchio (2015). We found an accretion disk luminosity of $L_{\text{Disk}} = 1.71 \times 10^{46} \text{ erg s}^{-1}$, falling at the upper end of the values estimated for γ -NLS1 ($\approx 1.69 \times 10^{46} \text{ erg s}^{-1}$, see Paliya et al. 2019). FSRQs typically exhibit even higher luminosities, on the order of $10^{47} \text{ erg s}^{-1}$ (see e.g., Ghisellini & Tavecchio 2015). One characteristic of γ -ray emitting NLS1s is the complexity of their X-ray emission, due to the possible contribution of the disk corona (not considered in our models), SSC emission, and EC emission. In our model, we find that the SSC component is crucial to fit the X-ray emission. We found that the jet power is dominated by the bulk motion of matter instead of Poynting flux ($P_e > P_B$), and is one order of magnitude larger than the disk luminosity. This composition of the jet power is found in FSRQ sources (see e.g., Ghisellini 2010b).

Although the fitting-derived parameters, such as those mentioned above, are not decisive in defining the classification of this source, they suggest that based on the modeling of the multifrequency SED, PKS 0440-00 shares more similarities with the FSRQ class. Therefore, if we consider that the $H\beta$ line is indicative enough for classifying the source as NLS1, we could suggest it as a potential hybrid source between the FSRQ and NLS1 classes. In Figure 6 we show the posterior distribution of the jet power components derived from the MCMC fit, compared to values reported in the literature for a sample of γ -NLS1, γ -CSS, and FSRQ (for the MCMC plot see Appendix A3).

6.4 Accretion-jet power

The results of our models can be used to explore the connection between accretion power and the energetic budget of the jet, and the implications in terms of a model-dependent classification. We follow the approach of Ghisellini et al. (2014) and, in Figure 8, we present the jet radiative power as a function of the accretion disk luminosity (left panels), and the total jet power as a function of the total accretion power (right panels). The power from our sources is computed as a posterior outcome from the MCMC sampler, hence the bar indicates the $2\text{-}\sigma$ confidence level from our modeling. We stress that this approach allows us to provide a better assessment of the power estimation when compared to large samples, showing an intrinsic dispersion. The data in the upper panels correspond to our three sources, together with the FSRQs and BL Lacs studied by Ghisellini et al. (2014). In the lower panels, we compare our sources with the sample of Paliya et al. (2017), where no distinction is made between FSRQs and BL Lacs, and we also include the γ -NLS1 studied by Paliya et al. (2019). It is well-established in blazars that the jet power is often comparable to or even exceeds the disk luminosity (Rawlings & Saunders 1991), anyhow, a model-dependent estimate of the jet power, or sample selection criteria, can lead to systematic biases, related to different features/assumptions in the underlying model or in the selected sample. Indeed, in the Ghisellini sample, most sources exhibit a P_{rad} lower than L_{Disk} , in contrast to the Paliya

sample, where sources are mainly distributed above the equality line, hence, it is worth comparing our sources to both the samples. Despite the aforementioned difference in P_{rad} , between the two samples, we notice that our sources occupy, for both the samples, a low radiative-power region, with $P_{\text{rad}} < L_{\text{Disk}}$ (see left panels of Figure 8, and top panels of Figure 9), except for the case of PKS 2004-447 model with $\theta = 9.5^\circ$. Interestingly, the distribution of our sources, both in the P_{rad} vs L_{Disk} and P_{jet} vs $\dot{M}c^2$ planes, falls within the region of γ -NLS1s limited by $P_{\text{rad}} \lesssim 10^{47} \text{ erg s}^{-1}$. Even though we notice that 3C 286 shows a very low P_{rad} compared to the L_{Disk} , consistently with earlier results obtained by Zhang et al. (2020) for the γ -CSS.

7 CONCLUSION

Our analysis of a sample of hybrid sources, based on the multi-wavelength SED numerical modeling and an MCMC sampling of the parameter spaces, allowed us to explore different physical parameters, useful in the classification of the sources, such as the jet orientation angle and the connection between the accretion disk and the jet power.

The main results of the multiwavelength analysis of the physical properties of our sources are summarized below.

- We found that PKS 2004-447 exhibiting a low Compton-dominated SED along with a relatively low L_{Disk} at a large viewing angle, can be modeled as an SSC-dominated object. In the case of an aligned jet with $\theta = 2^\circ$, the EC emission dominates the IC bump, in agreement with the presence of strong emission lines in the optical band. This might suggest that this source is in a transitional phase, either shifting from an efficient to an inefficient accretion mode or transitioning from a young to a more evolved state. The hybrid nature of this source is evident across different wavelengths.
- In the case of 3C 286, our findings indicate that using a one-zone model limits the viewing angle to $\sim 7^\circ$, mainly because of its impact on gamma-ray emission. In terms of the disk-jet connection, its behavior appears to resemble that of γ -NLS1, while the high magnetization of the jet is consistent with values found for γ -CSS sources, supporting the hybrid nature of the source. We plan a follow-up publication on this source, using more sensitive X-ray data to look for possible spectral signatures of corona emission, and the corresponding impact on the modeling.
- PKS 0440-00 exhibits characteristics common to both NLS1 and FSRQ classes. Our analysis indicates that the best fit is achieved when the emitting region is situated outside the BLR but within the DT. We note the importance of the SSC component in reproducing X-ray emission, as observed in some γ -NLS1s. However, a comprehensive examination of its optical spectrum is necessary to confirm its classification as NLS1. The presence of similarities with FSRQs and γ -NLS1 classes suggests the potentially hybrid nature of this source.

We plan a follow-up of this analysis, based on time-evolving modeling the presented SEDs, taking into account both the radiative and accelerating processes and the role of the jet adiabatic expansion, to provide a tighter constraint on the underlying physical scenario.

ACKNOWLEDGEMENTS

We thank the referee for insightful comments, which have significantly improved the manuscript. J.L.C and E.B. acknowledge support from DGAPA-PAPIIT UNAM through grant IN119123 and from

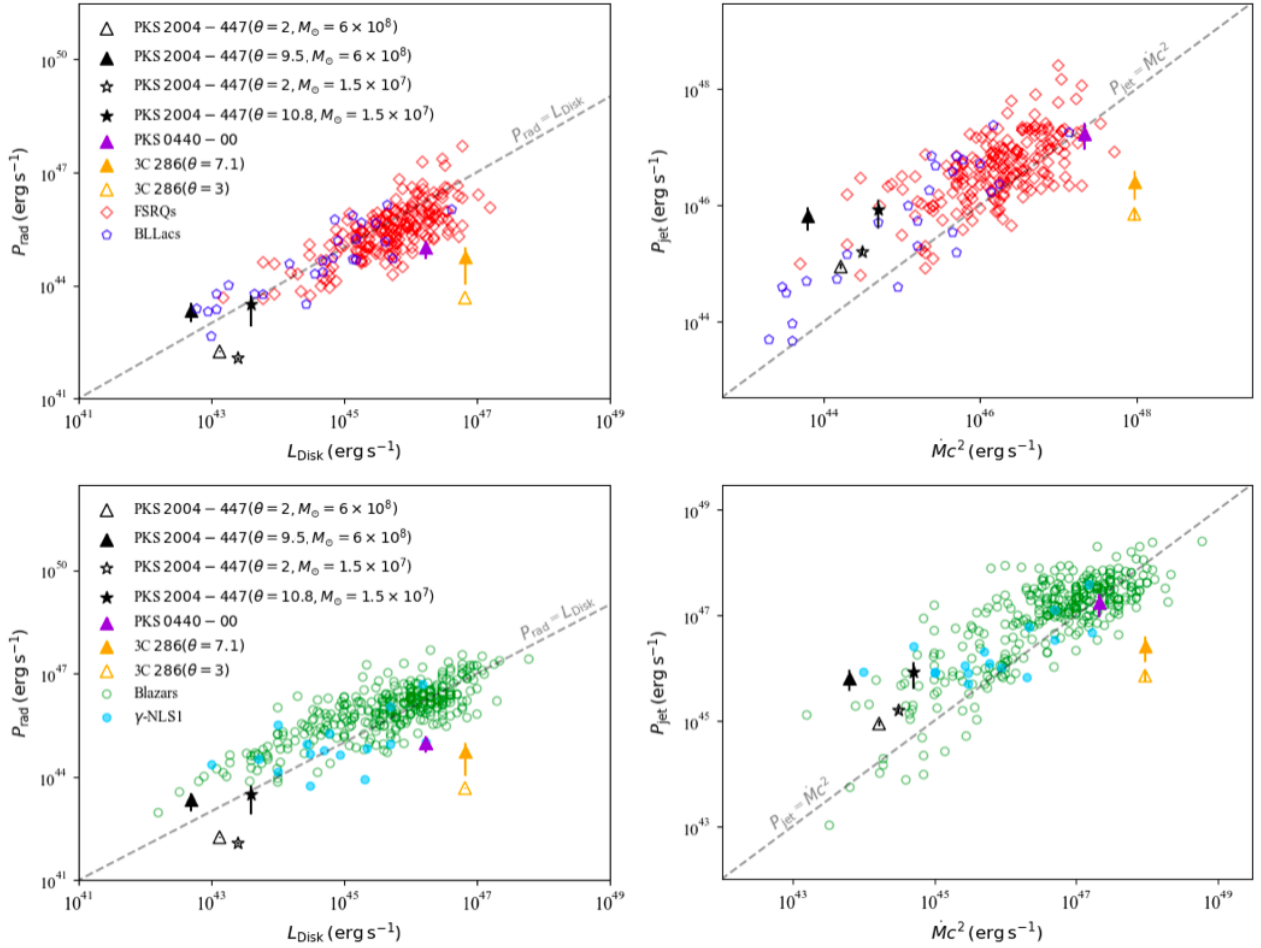


Figure 8. Left: Radiative jet power as a function of the accretion disk luminosity. Right: Total jet power as a function of the total accretion power, $\dot{M}c^2$ (assuming the accretion efficiency reported in the Tables 1, 2 and 3. As reported in the references, $\eta = 0.3$ for samples taken from the literature). Different symbols correspond to the values estimated from the different models of the sources. For comparison, in the top panels, we show the FSRQs, BL Lacs studied in Ghisellini et al. (2014), while the bottom panels show the so called gamma-loud blazars studied in Paliya et al. (2017) and the γ -NLS1 sample drawn from Paliya et al. (2019). The dashed line indicates the equality.

CONACYT Grant CF-2023-G-100. This research has made use of the NASA/IPAC Extragalactic Database (NED), which is operated by the Jet Propulsion Laboratory, California Institute of Technology, under contract with the National Aeronautics and Space Administration. This paper makes use of the following ALMA data: ADS/JAO.ALMA#2011.0.00001.CAL. ALMA is a partnership of ESO (representing its member states), NSF (USA) and NINS (Japan), together with NRC (Canada), MOST and ASIAA (Taiwan), and KASI (Republic of Korea), in cooperation with the Republic of Chile. The Joint ALMA Observatory is operated by ESO, AUI/NRAO and NAOJ. This publication makes use of data products from the Wide-field Infrared Survey Explorer, which is a joint project of the University of California, Los Angeles, and the Jet Propulsion Laboratory/California Institute of Technology, funded by the National Aeronautics and Space Administration. Part of this work is based on archival data, software or online services provided by the Space Science Data Center - ASI.

DATA AVAILABILITY

The multiwavelength archival data were taken from <https://tools.ssdc.asi.it/SED/>. ALMA data were taken from the public Calibrator Source Catalogue <https://almascience.eso.org/sc/>.

REFERENCES

- Abdo A. A., et al., 2009a, *ApJ*, **699**, 976
 Abdo A. A., et al., 2009b, *ApJ*, **707**, L142
 Abdo A., et al., 2010, *ApJ*, **716**, 30
 Abdollahi S., et al., 2020, *ApJS*, **247**, 33
 An T., Lao B. Q., Zhao W., Mohan P., Cheng X. P., Cui Y. Z., Zhang Z. L., 2017, *MNRAS*, **466**, 952
 Antonucci R., 1993, *ARA&A*, **31**, 473
 Baldi R. D., Capetti A., Robinson A., Laor A., Behar E., 2016, *MNRAS*, **458**, L69
 Begelman M. C., Blandford R. D., Rees M. J., 1984, *Reviews of Modern Physics*, **56**, 255
 Berton M., Foschini L., Ciroi S., Cracco V., La Mura G., Di Mille F., Rafanelli P., 2016, *A&A*, **591**, A88
 Berton M., et al., 2017, *Frontiers in Astronomy and Space Sciences*

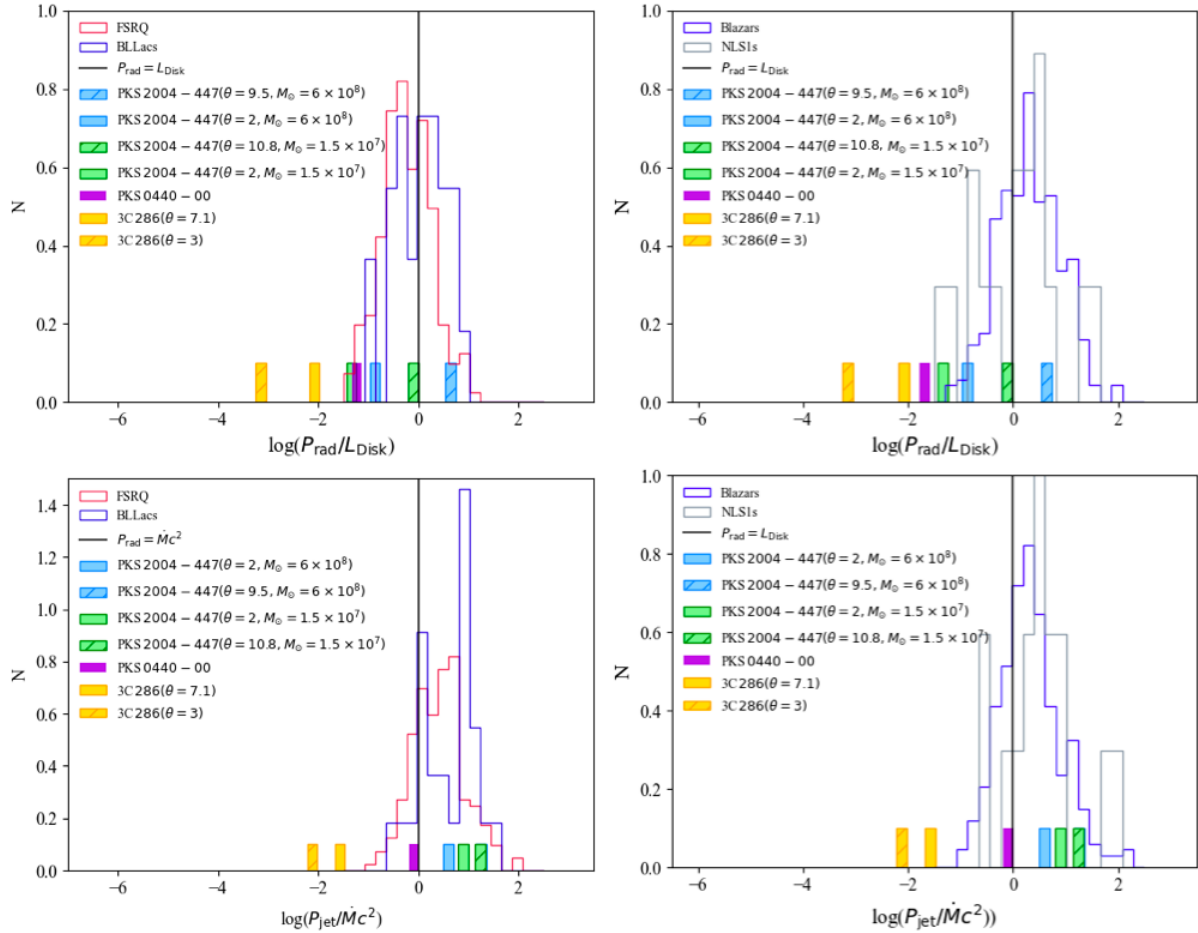


Figure 9. Top: Histograms of the $P_{\text{rad}}/L_{\text{Disk}}$ ratio. Bottom: Histograms of the $P_{\text{jet}}/\dot{M}c^2$ rate. Left: FSRQ and BL Lacs are shown as a comparison to our sources, drawn from Ghisellini et al. (2014). Right: Blazars and γ -NLS1 are sourced from Paliya et al. (2019). Bottom panels. The black line corresponds to equality.

Berton M., et al., 2021, *A&A*, 654, A125

Best P. N., Heckman T. M., 2012, *MNRAS*, 421, 1569

Blandford R. D., Rees M. J., 1978, in Wolfe A. M., ed., BL Lac Objects. pp 328–341

Blandford R. D., Znajek R. L., 1977, *MNRAS*, 179, 433

Blandford R., Meier D., Readhead A., 2019, *ARA&A*, 57, 467

Błażejowski M., Sikora M., Moderski R., Madejski G. M., 2000, *ApJ*, 545, 107

Böttcher M., 2007, *Ap&SS*, 309, 95

Celotti A., Ghisellini G., 2008, *MNRAS*, 385, 283

Chen Y., Gu Q., Fan J., Yu X., Ding N., Guo X., Xiong D., 2022, *MNRAS*, 517, 1381

Dembinski H., et al., 2023, scikit-hep/iminuit, doi:10.5281/zenodo.7750132, <https://doi.org/10.5281/zenodo.7750132>

Dermer C. D., 1995, *ApJ*, 446, L63

Edwards P., Tingay S., 2004, *A&A*, 424, 91

Fanti C., Fanti R., Dallacasa D., Schilizzi R., Spencer R., Stanghellini C., 1995, *A&A*, 302, 317

Finke J. D., 2013, *ApJ*, 763, 134

Finke J. D., 2016, *ApJ*, 830, 94

Foreman-Mackey D., Hogg D. W., Lang D., Goodman J., 2013, *PASP*, 125, 306

Foschini L., et al., 2017, *A&A*, 603, C1

Foschini L., et al., 2021, *Universe*, 7, 372

Franceschini A., Rodighiero G., Vaccari M., 2008, *A&A*, 487, 837

Frank J., King A., Raine D. J., 2002, *Accretion Power in Astrophysics: Third Edition*

Gallo L. C., et al., 2006, *MNRAS*, 370, 245

García-González J., et al., 2017, *MNRAS*, 470, 2578

Georganopoulos M., Kirk J. G., Mastichiadis A., 2001, *ApJ*, 561, 111

Ghisellini G., 2010a, in Maraschi L., Ghisellini G., Della Ceca R., Tavecchio F., eds, *Astronomical Society of the Pacific Conference Series Vol. 427, Accretion and Ejection in AGN: a Global View*. p. 249 (arXiv:0912.3258), doi:10.48550/arXiv.0912.3258

Ghisellini G., 2010b, in Bertin G., de Luca F., Lodato G., Pozzoli R., Romé M., eds, *American Institute of Physics Conference Series Vol. 1242, Plasmas in the Laboratory and the Universe: Interactions, Patterns, and Turbulence*. pp 43–54 (arXiv:1002.4619), doi:10.1063/1.3460151

Ghisellini G., 2013, *Radiative Processes in High Energy Astrophysics*. Vol. 873, doi:10.1007/978-3-319-00612-3,

Ghisellini G., Tavecchio F., 2008, *MNRAS*, 387, 1669

Ghisellini G., Tavecchio F., 2009, *MNRAS*, 397, 985

Ghisellini G., Tavecchio F., 2015, *MNRAS*, 448, 1060

Ghisellini G., Tavecchio F., Foschini L., Ghirlanda G., 2011, *MNRAS*, 414, 2674

Ghisellini G., Tavecchio F., Maraschi L., Celotti A., Sbarrato T., 2014, *Nature*, 515, 376

Gokus A., et al., 2021, *A&A*, 649, A77

Goodrich R. W., 1989, *ApJ*, 342, 224

Gu M., Chen Y., Komossa S., Yuan W., Shen Z., Wajima K., Zhou H., Zensus J. A., 2015, *ApJS*, 221, 3

Hardcastle M. J., Evans D. A., Croston J. H., 2007, *MNRAS*, 376, 1849

Kaspi S., Brandt W. N., Maoz D., Netzer H., Schneider D. P., Shemmer O., 2007, *ApJ*, 659, 997

- Kishimoto M., Hönig S. F., Beckert T., Weigelt G., 2007, *A&A*, **476**, 713
- Komossa S., 2018, in *Revisiting Narrow-Line Seyfert 1 Galaxies and their Place in the Universe*. p. 15 ([arXiv:1807.03666](https://arxiv.org/abs/1807.03666)), [doi:10.22323/1.328.0015](https://doi.org/10.22323/1.328.0015)
- Komossa S., Voges W., Xu D., Mathur S., Adorf H.-M., Lemson G., Duschl W. J., Grupe D., 2006, *AJ*, **132**, 531
- Merloni A., Heinz S., 2007, *MNRAS*, **381**, 589
- Meyer E. T., Fossati G., Georganopoulos M., Lister M. L., 2012, *ApJ*, **752**, L4
- Murgia M., Fanti C., Fanti R., Gregorini L., Klein U., Mack K. H., Vigotti M., 1999, *A&A*, **345**, 769
- Narayan R., Yi I., 1995, *ApJ*, **452**, 710
- Narayan R., Mahadevan R., Quataert E., 1998, in *Abramowicz M. A., Björnsson G., Pringle J. E., eds, Theory of Black Hole Accretion Disks*. pp 148–182 ([arXiv:astro-ph/9803141](https://arxiv.org/abs/astro-ph/9803141)), [doi:10.48550/arXiv.astro-ph/9803141](https://doi.org/10.48550/arXiv.astro-ph/9803141)
- O’Dea C. P., 1998, *PASP*, **110**, 493
- O’Dea C. P., Saikia D. J., 2021, *A&ARv*, **29**, 3
- Orienti M., D’Ammando F., Larsson J., Finke J., Giroletti M., Dallacasa D., Isacson T., Stoby Högland J., 2015, *MNRAS*, **453**, 4037
- Oshlack A., Webster R., Whiting M., 2001, *ApJ*, **558**, 578
- Osterbrock D. E., Pogge R. W., 1985, *ApJ*, **297**, 166
- Padovani P., 2017, *Nature Astronomy*, **1**, 0194
- Paliya V. S., Stalin C. S., Shukla A., Sahayanathan S., 2013, *ApJ*, **768**, 52
- Paliya V. S., Marcotulli L., Ajello M., Joshi M., Sahayanathan S., Rao A., Hartmann D., 2017, *ApJ*, **851**, 33
- Paliya V. S., Parker M. L., Jiang J., Fabian A. C., Brenneman L., Ajello M., Hartmann D., 2019, *ApJ*, **872**, 169
- Peacock J., Wall J., 1982, *MNRAS*, **198**, 843
- Planck Collaboration et al., 2014, *A&A*, **571**, A16
- Poutanen J., Stern B., 2010, *ApJ*, **717**, L118
- Rawlings S., Saunders R., 1991, *Nature*, **349**, 138
- Rees M. J., 1978, *Nature*, **275**, 516
- Sbarrato T., Ghisellini G., Maraschi L., Colpi M., 2012, *MNRAS*, **421**, 1764
- Sbarrato T., Padovani P., Ghisellini G., 2014, *MNRAS*, **445**, 81
- Schulz R., et al., 2016, *A&A*, **588**, A146
- Shaw M. S., et al., 2012, *ApJ*, **748**, 49
- Sikora M., Begelman M. C., 2013, *ApJ*, **764**, L24
- Tramacere A., 2020, *JetSeT: Numerical modeling and SED fitting tool for relativistic jets* (ascl:2009.001)
- Tramacere A., Giommi P., Perri M., Verrecchia F., Tosti G., 2009, *Astronomy & Astrophysics*, **501**, 879
- Tramacere A., Massaro E., Taylor A. M., 2011, *ApJ*, **739**, 66
- Urry C. M., Padovani P., 1995, *PASP*, **107**, 803
- Yao S., Komossa S., 2021, *MNRAS*, **501**, 1384
- Zeldovich Y. B., Novikov I. D., 1971, *Relativistic astrophysics. Vol.1: Stars and relativity*
- Zhang J., Zhang H.-M., Gan Y.-Y., Yi T.-F., Wang J.-F., Liang E.-W., 2020, *ApJ*, **899**, 2

APPENDIX A: MCMC FIT OF THE SED MODELS PRESENTED FOR EACH SOURCE

We present the MCMC fit to the observed data, using parameters derived from the frequentist best-fit model as a starting point. We set flat priors for the MCMC, centered on the best-fit values. For each source, we selected a subset of parameters that significantly influence the understanding of their impact on EC emission and jet orientation. For these parameters, we generated posterior contour maps and posterior distributions. The posterior distributions are plotted with vertical dashed lines indicating the selected quantiles: 0.16, 0.5, and 0.84.

This paper has been typeset from a $\text{\TeX}/\text{\LaTeX}$ file prepared by the author.

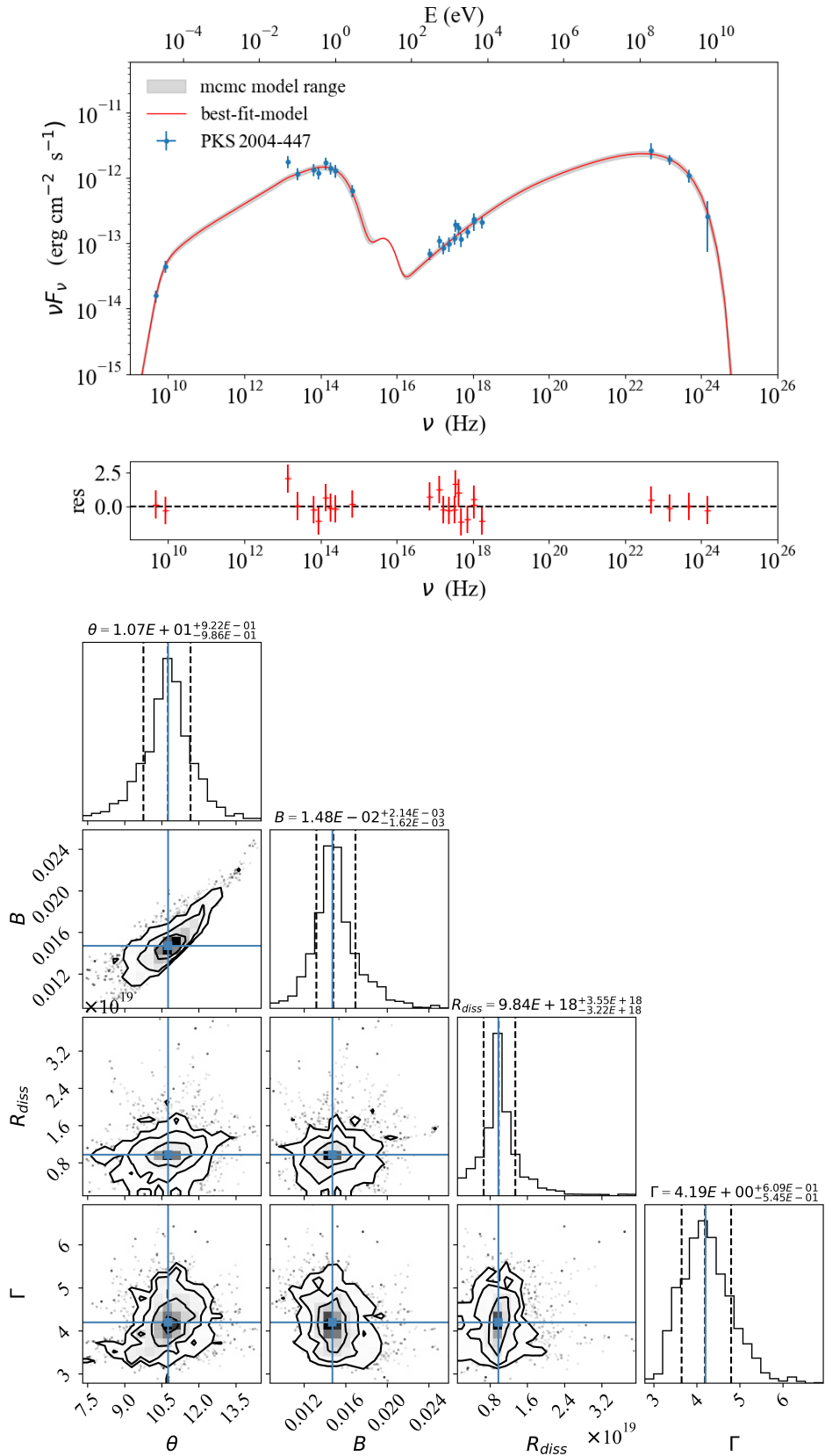


Figure A1. Top panel: MCMC fit to the SED of PKS 2004-447. The prior distribution is flat and centered on the best-fit values of the model shown in the right bottom panel of Figure 1. Bottom panel: Posterior contour maps illustrating correlations among a sub-sample of parameters. Due to our interest in exploring the impact of the jet orientation and the location of the emitting region, we selected the viewing angle θ , the bulk Lorentz factor, the magnetic field, and the distance from the black hole to the emitting region to generate the posterior contour maps and posterior distribution. There is a strong correlation between the magnetic field (B) and the viewing angle (θ).

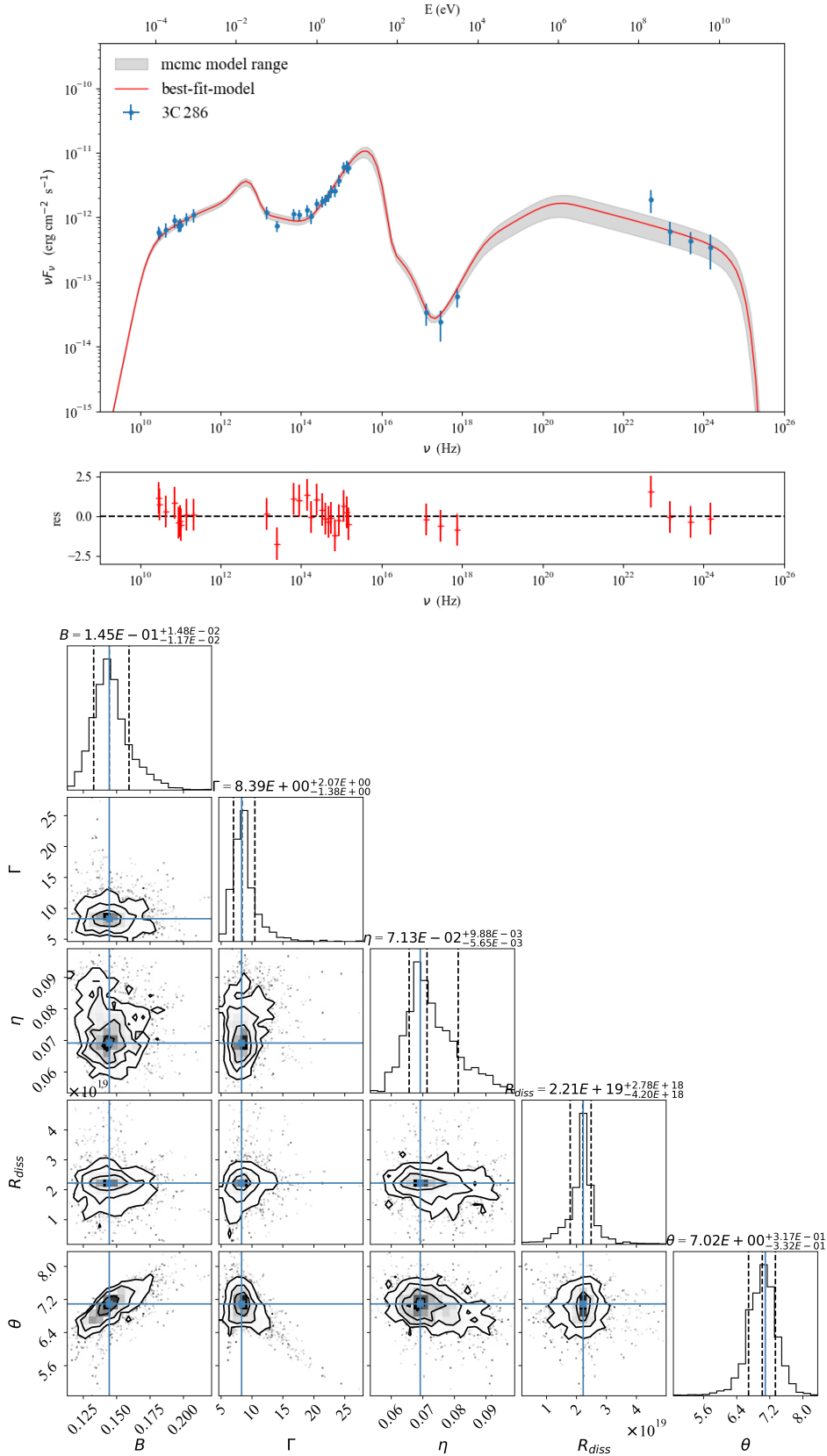


Figure A2. Top panel: MCMC fit to the SED of 3C 286. The prior distribution is flat and centered on the best-fit values of the model shown in the bottom panel if Figure 3. Bottom panel: Posterior contour maps illustrating correlations among a sub-sample of parameters. In order to explore the impact of the jet orientation and accretion disk parameters, we selected the following parameters to generate the posterior contour maps and distribution: the magnetic field, the bulk Lorentz factor, accretion efficiency, the distance from the black hole to the emitting region, and viewing angle. There is an observed correlation between B and θ .

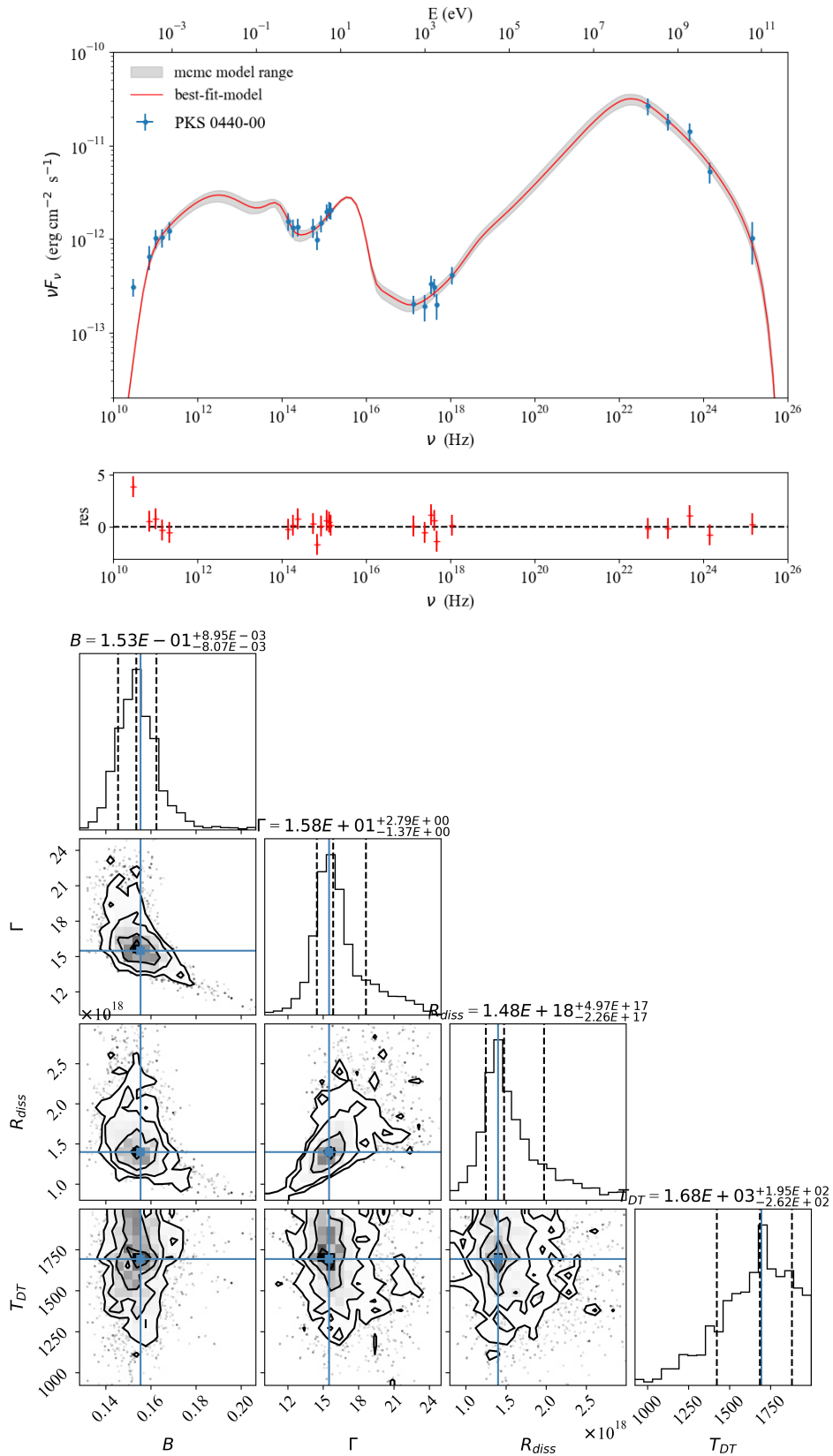


Figure A3. Top panel: MCMC fit to the SED of PKS 0440-00. The prior distribution is flat and centered on the best-fit values of the model shown in the top panel of Figure 5. Bottom panel: Posterior contour maps illustrating correlations among a sub-sample of parameters. For this source, we generate the posterior contour maps and posterior distribution of the position of the emitting region along the jet, the magnetic field, and the bulk Lorentz factor, as well as the temperature of the dusty torus. There is an observed correlation between the position of the emitting region along the jet (R_{diss}) and the bulk factor (Γ), and an anticorrelation between the latter and B .